Multiplexed neuromodulatory-type-annotated whole-brain EM-reconstruction of larval zebrafish

Fu-Ning Li[1,6], Jia-Zheng Liu[2,6], Can Shi[1,4,6], Jing-Bin Yuan[2,3,6], Ya-Nan Lv[2,3,6], Jing Liu[2,6], Li-Na Zhang[2,6], Lin-Lin Li[2,6], Li-Jun Shen[2,6], Xi Chen[2,6], Hao Zhai[2,3], Yan-Chao Zhang[2,3], Rong-Kun Tao[1], Han-Yang Hu[1], Fang-Xu Zhou[2], Tong Xin[2], Bo-Hao Chen[2,3], Hao-Ran Chen[2,3], Sheng Chang[2], Hong-Tu Ma[2], Hai-Yang Yan[2,3], Jia-Liang Zu[1,3], Jin-Yue Guo[2,3], Zheng-Huan Fang[1], Xiao-Hui Dong[2], Li-Mei Lin[2], Xing-Hui Zhao[2], Chen-Ying Qian[1], Yan-Song Wang[1,3], Shi-Rong Jin[1], Chang-Mei Zhang[1], Pei-Shan Xiang[1,4], Yong-Xin Yang[1,4], Yu Qian[1,3], Yu-Chen Gong[1,3], Xu-Fei Du[1], Qi-Wei Xie[2], Hua Han[2,3,*] & Jiu-Lin Du[1,3,4,5,*]

[1] Institute of Neuroscience, State Key Laboratory of Brain Cognition and Brain-Inspired Intelligence Technology, Center for Excellence in Brain Science and Intelligence Technology, Chinese Academy of Sciences, 320 Yue-Yang Road, Shanghai 200031, China

[2] State Key Laboratory of Brain Cognition and Brain-Inspired Intelligence Technology, Institute of Automation, Chinese Academy of Sciences, Beijing 100190, China

[3] School of Future Technology, School of Artificial Intelligence, University of Chinese Academy of Sciences, Beijing 101408, China

[4] University of Chinese Academy of Sciences, 19A Yu-Quan Road, Beijing 100049, China

[5] School of Life Science and Technology, ShanghaiTech University, 319 Yue-Yang Road, Shanghai 200031, China

[6] These authors contributed equally

* These authors jointly supervised this work: Hua Han (hua.han@ia.ac.cn), Jiu-Lin Du (forestdu@ion.ac.cn)

Electron microscopy (EM)-based reconstruction of microscopic connectomes is crucial in elucidating the synaptic organization of the brain architecture[1-10]. To understand the reconstructed connectome and integrate it with functional interrogation, it is indispensable to identify neuronal types in EM datasets[11-14]. Among the vast array of neuronal types, diverse evolutionarily-conserved neuromodulatory (NM) neurons endow the hardwired brain architecture with flexible neural processing and function[15-18]. Here, we present Fish-X, a synapse-level, multiplexed NM-type-annotated reconstruction spanning the retina, brain and anterior spinal cord (SC) of a 6-day-old larval zebrafish, capturing >176,000 cells and >25 million synapses in the brain and SC. Among diverse neuronal types, NM (including noradrenergic (NE), dopaminergic (DA), serotonergic (5HT), and hypocretinergic) and glycinergic neurons are identified via subcellular localization of the enhanced ascorbate peroxidase-2[19], while excitatory (E) glutamatergic and inhibitory (I) GABAergic neurons are inferred through morphology comparison with the Zebrafish Mesoscopic Atlas[20]. Different types of NM neurons display various synapse density and number on dendrites, with the number being positively correlated with their total projection length. By reconstructing presynaptic neurons (PNs) and identifying their E/I identity, in-depth analysis of individual locus coeruleus (LC)-NE neurons revealed that they receive brain-wide synaptic inputs, which are organized into modality- and E/I-dependent spatial patterns along dendrites. Moreover, a subset of PNs innervate multiple LC-NE neurons, and this input sharing extends across NE, DA, and 5HT systems, suggesting a co-innervation mechanism for coordinated modulation within and across diverse NM systems. Thus, our study reveals the multi-dimensional synaptic input organization of the LC-NE system. Integrated with the zebrafish mesoscopic atlases[20,21], the Fish-X offers a valuable resource for deciphering how, at the level of synaptic architecture, NM systems interact with sensorimotor pathways to shape neurocomputing in the larval zebrafish brain.

Brain function is underpinned by exquisitely organized architecture that operates across various scales, ranging from the precise spatial localization of synapses to the intricate morphologies of individual neurons and the characteristic neural connectivity among distinct regions. The synaptic-resolution connectome, representing a foundational challenge in neuroscience, offers a mechanistic framework to bridge structure and function[13,14,22-25]. While complete wiring diagrams of the nervous system have been achieved for small invertebrate animal models, including *Caenorhabditis elegans* and *Drosophila melanogaster*[1,3-5,7,8], vertebrate whole-brain connectomes remain incomplete—despite landmark achievements in mouse and human cortical reconstructions[9,10,26-30]. Zebrafish (*Danio rerio*) larvae emerge now as the most tractable vertebrate model for whole-brain reconstruction, combining manageable brain scale with conserved neural architecture. Pioneering work has mapped local

circuits[22,25,31-33] or generated whole-brain datasets[2,6,34], yet existing datasets often possess limited resolution or omit essential input-output regions—notably the retina (vision entry) and spinal cord (SC, motor output) — limiting systems-level interrogation of sensorimotor transformation.

The functional complexity of neural networks arises not only from their physical wiring, but also from the molecular diversity of their constituent neurons. Molecularly defined neuronal types serve as crucial bridges linking static structural data with functional readouts[11-14]. Recent light-microscopy-based connectomics highlights an urgent need for molecular annotated connectomes[35]. Traditional electron microscopy (EM)-based connectomics primarily relies on prior structural features for neuronal identification, including stereotyped soma locations, projection morphologies, specialized cellular features, and synaptic ultrastructures[2,24,31,36,37]. For neuronal populations with less well-characterized structural signatures, neuronal type identification has been achieved mainly through correlative light-electron microscopy (CLEM)[34], genetically encoded tags for EM (GETEM)[38-40] and immuno-EM[41]. Beyond a few well-studied excitatory and inhibitory neuronal populations (e.g., cortical pyramidal neurons in mouse, reticulospinal neurons in zebrafish), the majority of cell types, particularly neuromodulatory (NM) populations, lack sufficient ground-truth data for structural feature extraction. For these challenging cases, GETEM represents a highly feasible annotation approach, enabling precise neuronal type identification within synaptic-resolution wiring diagrams.

Therefore, we build Fish-X, a whole-brain, synapse-level, multiplexed molecular annotated serial-section EM (ssEM) dataset spanning from the retina to the anterior SC in 6-day post-fertilization (dpf) larval zebrafish. In the brain, soma and neuropil regions are spatially segregated. Most brain regions display heterogeneity in synapse density, yet exhibit comparable lognormal distributions of synapse strength. Diverse types of NM neurons, including noradrenergic (NE), dopaminergic (DA), serotonergic (5HT), and hypocretinergic (Hcrt) neurons, and glycinergic (Gly) neurons are identified using the enhanced ascorbate peroxidase-2 (APEX2) targeted to distinct subcellular compartments, driven by neuronal-type-specific promoters[11,19,42,43]. Besides, Excitatory (E) glutamatergic (Glu) and inhibitory (I) GABAergic (GABA) neurons are inferred through the Zebrafish Mesoscopic Atlas[20]-assisted morphology comparison. Leveraging this unique advantages of the multiplexed molecular annotated ssEM dataset, we investigated perisomatic characteristics across neuronal types, with focus on monoaminergic neurons, including NE, DA, and 5HT neurons. Heterogeneous ultrastructural features extracted from genetically-labeled ground truth enable identification of unlabeled neurons both in this study and other zebrafish connectome datasets.

Morphologically diverse NM neurons innervate various sensory – motor brain regions. Whereas some NM systems exhibit localized innervation for local regulation, others possess widespread projections enabling multi-regional modulation[44-48]. Through brain-wide

synapse-level reconstruction, we tackled fundamental questions concerning the bi-pathway brain architecture composed of NM pathways and sensorimotor pathways[15-18,49,50]: where NM neurons receive upstream inputs and how these inputs are spatially organized at the synaptic level. To this end, we focused on the locus coeruleus (LC)-NE system, because it serves as a pivotal hub for brain-wide activity regulation[48,51-58]. We found that an individual LC-NE neuron receives brain-wide synaptic inputs with modality- and strength-specific spatial organization. Furthermore, we revealed the distinct-yet-overlapping organization of synaptic inputs on LC-NE neurons. Intriguingly, different monoaminergic systems also share common inputs, suggesting a modular input architecture that coordinates NE, DA, and 5HT modulation.

Fish-X offers a valuable synapse-level, whole-brain resource featuring a variety of precisely annotated molecularly defined neuronal types. Together with other whole-brain zebrafish EM datasets that provide E/I annotations and calcium activity functional profiles[6,34], Fish-X contributes to the foundational infrastructure that encompasses sample preparation, algorithms, proofreading platforms, and public sharing. This infrastructure is essential for future whole connectome reconstruction. Furthermore, Fish-X demonstrates synergistic potential with multimodal zebrafish mesoscopic datasets[20,59]. It not only enhances the annotation of neuronal types in EM connectomes but also facilitates the analysis of synaptic connectivity among specific neurons, with their morphology traced in functional studies. Collectively, Fish-X serves as a critical reference for deciphering the principles of synaptic organization within the brain bi-pathway architecture.

Whole-brain ssEM of APEX2-labeled larval zebrafish

We utilized APEX2, which catalyzes hydrogen peroxide (H_2O_2)-dependent polymerization and localized deposition of diaminobenzidine (DAB)[19], to enable EM labeling of molecularly defined neuronal types. To achieve multiplexed labeling within a single brain preparation, we expressed APEX2 in distinct neuronal types using cell-type-specific promoters, and targeted it to distinct subcellular compartments via corresponding signal peptides. Thus, we generated the zebrafish line, *Gt(vmat2:GAL4FF);Tg(dbh:GAL4FF;UAS:cytosol-APEX2-TagRFP);Tg(hcrt:APEX2-TagRFP-NLS);Tg(glyt2:MITO-APEX2-TagRFP)*, in which APEX2 conjugated with TagRFP was specifically targeted to (i) the cytoplasm in monoaminergic neurons (including NE, DA, and 5HT neurons), (ii) the nucleus in Hcrt neurons, and (iii) the mitochondria in Gly neurons (Fig. 1a and Extended Data Fig. 1; see Methods). By immunohistochemical staining and crossing with neuronal type-specific reporter fish lines, we confirmed that the APEX2 line successfully labeled target neurons in specific nuclei: including NE neurons in the LC and medulla oblongata (MO), DA neurons in the olfactory bulb (OB), posterior tuberculum (PT) and caudal hypothalamus (Hc), 5HT neurons in the pretectum (Pr) and raphe nucleus (RN), Hcrt neurons in the hypothalamus (Hyp), and Gly neurons across the brain and SC, with varying

142 labeling efficiency (Extended Data Fig. 1b-d). This labeling variability may result from
143 differential APEX2 expression levels caused by random insertion of genetic sequences in the
144 Tol2-based transgenic system.

145 Using the automated tape-collecting ultramicrotome – scanning electron microscopy
146 (ATUM-SEM) approach[2,60], we acquired a whole-brain ssEM dataset at $4 \times 4 \times 33$ nm^3 per
147 voxel resolution along the rostrocaudal axis, extending from the olfactory epithelium to the
148 anterior SC (vertebra 1) and including the right retina in a 6-dpf multiplexed APEX2-labeled
149 larva (Extended Data Fig. 2a; see Methods). The imaged volume, generated from 22,887
150 consecutive coronal-view ultrathin sections, encompassed ~3.1160×10^7 μm^3 for the entire
151 brain and anterior SC, ~5.5620×10^4 μm^3 for the right optic nerve, and ~6.0877×10^6 μm^3 for
152 the right retina (Fig. 1b).

153 We validated 176,810 cells in the brain and anterior SC through convolutional neural
154 network (CNN)-based three-dimensional (3D) automated nucleus segmentation (see
155 Methods), with subsequent manual proofreading. In addition, manual cell counting in the
156 right retina yielded 70,910 cells. Furthermore, we automatically segmented 25.25 million
157 postsynaptic densities (PSDs), 15.77 million synaptic vesicle (SV) clouds, and 13.73 million
158 mitochondria in the brain, respectively (see Methods). At the macroscopic level, the brain
159 exhibited a bilaterally symmetrical architecture. Among neural tracts, which serve as
160 highways for inter-regional signal transmission, only the reticulospinal system[2], lateral line
161 system[2], and optic nerve (partially) displayed significant myelination (Fig. 1b,c). Besides, the
162 vascular network was predominantly localized within neuropils (77.78% of the relevant
163 reconstructed volume) (Fig. 1c). In general, somata were predominantly localized in the
164 medial-dorsal regions (94.59% of the total cell population), while the lateral-ventral neuropils
165 contained sparse somata and provided spaces for synaptic connections (Fig. 1d,e). Using a
166 CNN-based approach, we generated automated 3D reconstructions of the brain and anterior
167 SC (Extended Data Fig. 2b,c; see Methods). Manually reconstructing morphologies of
168 brain-wide neurons including APEX2-labeled NM and Gly neurons, was then performed
169 using a custom collaborative proofreading software (see Methods). We reconstructed the
170 morphology of 523 neurons, encompassing 9 types: APEX2-labeld NE, DA, 5HT, Hcrt, and
171 Gly neurons, as well as Glu neurons, GABA neurons, retinal ganglion cells (RGCs), and a
172 Mauthner cell (M-cell) (Fig. 1f and Supplementary Video 1; see Methods). The identities of
173 the latter four types were determined through alignment with the Zebrafish Mesoscopic
174 Atlas[20] (see below in Fig. 2) or using their distinct morphological properties.

175

176 **Neuronal type identification via multi-strategy approaches**

177 For neuronal type identification, we first employed a CLEM approach to align the ssEM
178 dataset with the region-annotated brain template in the Zebrafish Mesoscopic Atlas[20],
179 followed by identification via multi-strategy approaches (Fig. 2a, Extended Data Fig. 2a, and
180 Supplementary Table 1; see Methods). All cells in the brain and retina were mapped to their

181 corresponding regions. Significant variations in soma density were observed across regions
182 (Extended Data Fig. 3a,b and Supplementary Table 2). In the brain, the neuropil layer (NL)
183 and periventricular cell layer (PL) in the optic tectum exhibited the minimum and maximum
184 soma densities (0.51 *vs* 10.62 per 10^3 μm^3), respectively. In the retina, the outer nuclear layer
185 (ONL), the inner nuclear layer (INL), and retinal ganglion cell layer (RGCL) showed higher
186 soma densities (12.18, 21.01, and 15.63 per 10^3 μm^3, respectively; Extended Data Fig. 3a,b
187 and Supplementary Table 2).

188 We integrated distinct EM-visible labeling signatures with soma location to identify
189 APEX2-labeled neurons (Fig. 2a, top). As different types of monoaminergic nuclei are
190 discretely localized, we discriminated neurons as NE, DA, or 5HT based on their soma
191 location, together with *vmat2*-driven cytoplasmic APEX2 labeling. Hcrt and Gly neurons
192 were identified based on nuclear and mitochondrial APEX2 labeling, respectively. In total, we
193 identified at least five molecular types across 9 nuclei/regions ($n_{LC\text{-}NE}$ = 12, $n_{MO\text{-}NE}$ = 54,
194 $n_{OB\text{-}DA}$ = 38, $n_{PT\text{-}DA}$ = 22, $n_{Hc\text{-}DA}$ = 45, $n_{Pr\text{-}5HT}$ = 9, $n_{RN\text{-}5HT}$ = 117, n_{Hcrt} = 12, and n_{Gly} = 4,019),
195 with a total number of 4,328 neurons (Fig. 2b, Extended Data Figs. 1a and 4, and
196 Supplementary Video 2). Due to the abundant population of Gly neurons, we trained a neural
197 network to automatically segment APEX2-labeled mitochondria and subsequently identified
198 Gly neurons based on the property and number of APEX2-labeled mitochondria within their
199 somata (see Methods). Other APEX2-labeled neurons were manually quantified by expert
200 proofreaders.

201 By integrating deep-learned and traditional features, we systematically investigated the
202 morphologies of whole-brain cellular nuclei and revealed generally continuous distributions
203 in clustering space, though vasculature-associated cell types (e.g., endothelial cells, EC;
204 pericytes, PC) tended to aggregate (Extended Data Fig. 3c). Neuronal nuclei typically
205 exhibited spherical or ellipsoidal morphologies, compared with the flattened, sheet-like nuclei
206 of vasculature-associated cells and the irregular shapes observed in some undefined cell types.
207 Among APEX2-labeled neurons, some types (e.g., LC-NE and PT-DA neurons) displayed
208 larger nuclei, and some possessed nuclei with shallow grooves (e.g., LC-NE neurons) or deep
209 infoldings (e.g., Gly neurons) (Extended Data Fig. 3d).

210 Next, we tested whether structural features extracted from APEX2-labeled neurons could
211 serve as ground truth to identify corresponding types of neurons without APEX2 labeling (Fig.
212 2a, middle). Due to the incompleteness of most cells after automated reconstruction,
213 identification using local structural features enables rapid targeting of specific neuronal
214 populations, followed by proofreading[36,37]. For instance, LC-NE neurons exhibited not only
215 larger nucleus volumes but also larger somata, extensive endoplasmic reticulum (ER), a
216 quantity of mitochondria, and a specialized cilium (Fig. 2c). Quantitative analysis revealed
217 that, compared with adjacent randomly selected cells, LC-NE neurons had a lower
218 nucleus-to-soma volume ratio (LC-NE neuron *vs* adjacent cell: 0.4123 ± 0.0808 *vs* 0.6530 ±
219 0.0113, $P < 0.05$, Mann Whitney test) and a higher somatic mitochondrial density (LC-NE

220 neuron *vs* adjacent cell: 0.5449 ± 0.0496 *vs* 0.0843 ± 0.0088 per 1 μm^3, $P < 0.001$, Mann
221 Whitney test) (Fig. 2d and Supplementary Table 3). These distinct perisomatic features
222 enabled precise discrimination between NE and non-NE cells within the LC region.
223 Subsequent clustering analysis integrating both nucleus and soma characteristics further
224 validated this observation (Fig. 2e). Based on these criteria, we identified an additional
225 unlabeled LC-NE neuron in the right hemisphere (blue arrow in Fig. 2d,e), whose
226 morphological features closely matched those of the APEX2-labeled LC-NE neurons (Fig. 2f).
227 We extended this analysis to other APEX2-labeled neuronal types and found that only PT-DA
228 neurons could be identified based solely on local perisomatic features (Extended Data Fig. 3g
229 and Supplementary Table 3). The remaining neuronal types exhibited no significant
230 ultrastructural differences from adjacent cells (Extended Data Fig. 3e,f,h-l and Supplementary
231 Table 3), further highlighting the value of APEX2 labeling for precise neuronal type
232 identification.

233 Given that Glu and GABA neurons are fundamental elements of the brain, we
234 investigated whether the synaptic ultrastructure and neuronal morphology can be used for E/I
235 type identification of other neurons without APEX2 labeling in the Fish-X dataset. Glu and
236 GABA synapses typically exhibit asymmetrical and symmetrical structures, and differ in PSD
237 thickness in mammalian brains[61]. By using two additional EM datasets with mitochondrial
238 labeling either in Glu or GABA neurons, we found that Glu and GABA synapses showed no
239 significant differences in both the thickness and volume of PSDs, with only minor exceptions
240 in rare individual cases (Extended Data Fig. 5), suggesting that synapses in zebrafish may not
241 follow the criterion observed in mammals. Then we pursued neuronal type inference via
242 morphology comparison with fully-reconstructed E and I neurons from the Zebrafish
243 Mesoscopic Atlas[20] (n_{Glu} = 12,219, n_{GABA} = 5,371, n_{Gly} = 2,193) (Fig. 2a, bottom). EM query
244 neurons were pre-registered to the mesoscopic brain template through a CLEM pipeline
245 (Extended Data Fig. 2a; see Methods), followed by the extraction of mesoscopically traced
246 neurons within a 25-μm radius sphere centered at the query neuron's geometric centroid.
247 Subsequent skeleton matching against these references yielded penalty scores (see Methods).
248 For each EM query neuron, mesoscopic references with a lower penalty score are
249 theoretically more similar. Top-ranked results were further manually verified to categorize all
250 467 EM query neurons as matched or unmatched. Among 467 queries, 389 of them were
251 successfully matched to morphologically similar E or I counterparts (Fig. 2g,h). Meanwhile,
252 78 queries exhibited obvious differences in morphology with top-ranked references (Fig. 2i),
253 calling for the needs for more complete reconstructions of these EM neurons and more
254 coverage of the mesoscopic atlas. In general, matched queries showed a lower penalty score
255 than unmatched ones (Fig. 2j; $P < 0.0001$, Mann Whitney test), suggesting the efficiency of
256 morphology comparison. Among 56% (219/389) of matched queries, their top-ranked
257 references were predominantly of a single E or I type (E/I-specific match). The remaining
258 queries (170/389) displayed top-ranked references with mixed E/I types and could not be

259 specifically inferred (E/I-ambiguous match). For instance, the EM query neuron #41 exhibited
260 similar morphology with both Glu, GABA, and Gly neurons, resulting in the uncertainty of
261 E/I inference based on morphological comparison (Fig. 2k). However, this query was reliably
262 identified as a Gly neuron due to its mitochondrial APEX2 labeling (Fig. 2l), again showing
263 the critical value of APEX2 labeling in neuronal type identification.
264
265 **Region- and NM type-distinctive profiles of synapse distribution**
266 To investigate the connectivity properties of diverse neuronal types, we first systematically
267 examined the distribution of all synapse-related components across brain regions. The results
268 revealed highly consistent patterns of brain-region-level distributions across PSDs, SVs and
269 mitochondria (Extended Data Fig. 6, Supplementary Tables 4,5,6, and Supplementary Video
270 3). To further investigate the synapse-level co-localization among these three components
271 (Fig. 3a,b), we identified the automatically-segmented presynaptic and postsynaptic
272 supervoxels of individual PSDs, while assigning SVs and mitochondria to their respective
273 associated supervoxels. We found that 93.5% of PSDs co-localized with SVs, whereas only
274 59.2% of PSDs co-localized with presynaptic mitochondria (Fig. 3a, top). Consistently, 84.3%
275 of SVs and 61.3% of mitochondria distributed in presynaptic sites of synapses defined by
276 PSDs, respectively (Fig. 3a, middle and bottom).
277 To minimize interference from misidentified instances in automated segmentation results,
278 we defined typical synapses by the co-occurrence of SVs at presynaptic sites and PSDs at
279 postsynaptic sites. The density of typical synapses varied across brain regions (Fig. 3c), and
280 was negatively correlated with soma density (Fig. 3d; $R^2 = 0.7070$, $P < 0.0001$), reinforcing
281 their spatial segregation within the brain. Interestingly, when we incorporated features
282 associated with synapse strength (e.g., the volumes of PSDs, SVs, and mitochondria) into
283 analysis, we found that all three synapse strength-related characteristics followed comparable
284 lognormal distributions across brain regions (Fig. 3e-h). Some regions, such as the epiphysis
285 (Ep, Fig. 3f) and lobus caudalis cerebelli (LCa, Fig. 3h), exhibited sharply peaked PSD
286 volume distributions, suggesting potential variations in synaptic organization.
287 Extensive research showed that the axonal innervation patterns of diverse NM systems
288 vary in the degree of brain-wide projections[44-48]. A similar result was revealed by single-cell
289 morphological tracing in 6-dpf larval zebrafish (Extended Data Fig. 7). Among NM systems,
290 LC-NE neurons displayed widespread broadcasting axonal projections throughout the brain,
291 while other types (e.g., OB-DA neurons) exhibited spatially restricted innervation. To
292 examine the synaptic input profile at NM neurons' dendrites, a topic which remains
293 understudied in the field, we manually reconstructed somatodendritic morphologies for
294 multiple types of NM neurons in the right hemisphere as well as Gly neurons and validated
295 their presynaptic input sites (Fig. 3i,j and Supplementary Video 4). We found that the soma of
296 most NM neurons received few synaptic inputs, compared with the well-studied M-cell that
297 received substantial synaptic inputs on its soma (Extended Data Fig. 8 and Supplementary

Video 5). In total, we verified 6,812 synaptic inputs for 44 APEX2-labeled neurons, including 5 LC-NE neurons, 3 MO-NE neurons, 3 OB-DA neurons, 4 PT-DA neurons, 3 Hc-DA neurons, 3 Pr-5HT neurons, 4 RN-5HT neurons, 2 Hcrt neurons, as well as 17 Gly neurons (Fig. 3i,j). Dendrites were manually identified based on synaptic input locations for the subsequent calculation of dendritic input densities. These neuronal types displayed diverse synapse density on dendrites (Fig. 3k). In particular, the three types of monoaminergic NM neurons—LC-NE, PT-DA, and RN-5HT—collectively exhibited a higher average synaptic input density. Notably, the number but not the density showed a positive correlation with their total projection length (Fig. 3l,m).

Synaptic input organization of the LC-NE system

A fundamental question in the study of NM systems concerns the origin and spatial organization of their presynaptic inputs at dendrites, as elucidating these principles is essential for understanding their activity dynamics and regulatory physiology[18,62]. To address this, we investigated the LC-NE system, a key node for regulating brain-wide neural networks. While prior viral-genetic tracing studies in mammals mapped the diverse brain-wide origins of inputs to LC-NE neurons, revealing convergent organization at a cellular level[45,46], a critical question remains unanswered: how are these functionally distinct inputs spatially organized at the dendrite of LC-NE neurons?

Therefore, we initiated our tracing from all identified synaptic input sites of the LC-NE neuron #3, which exhibited the longest dendrites (~1.812 mm) and the highest dendritic input indegree ($n_{synapse}$ = 560) among all five APEX2-labeled LC-NE neurons in the right hemisphere (Fig. 4a,b, Extended Data Fig. 9a,b, and Supplementary Video 4). We successfully traced 418 synaptic inputs back to 374 presynaptic neurons (PNs)' somata, with 182 synapses from 160 PNs in sensory- or sensory relay-related regions, and 236 synapses from 214 PNs in motor-related regions (Fig. 4c). These PNs widely distributed across 32 out of 52 brain regions (Fig. 4d and Supplementary Video 6). In comparison, OB-DA neurons' PNs were spatially restricted, while PT-DA and RN-5HT neurons also received inputs from widely distributed PNs (Extended Data Fig. 10). Combinatorial analysis of the dendritic position of synaptic sites and the soma location of corresponding PNs showed that the LC-NE neuron implemented modality-dependent spatial organization of synaptic inputs at their dendrites. Specifically, sensory-related (including sensory relay) and motor-related inputs preferentially targeted more distal or proximal dendrites of these neurons, respectively (Fig. 4e; path length to the soma: sensory-related, 122.8 ± 3.2 μm *vs* motor-related, 103.3 ± 2.5 μm; $P < 0.001$, Mann Whitney test). Similar phenomena were observed in other four LC-NE neurons (Extended Data Fig. 9c). Furthermore, both sensory- and motor-related inputs exhibited a spatial gradient of synaptic strength, with increasing volumes of PSDs and SVs when approaching the soma (Fig. 4f,g). Meanwhile, the strength distributions of these two input types were comparable (Fig. 4f,g). Furthermore, based on morphology comparison and

337 APEX2-labeling (see Fig. 2), we inferred the E/I identity of 188 PNs among all 374 PNs
338 ($n_{sensory\text{-}Glu}$ = 60, $n_{sensory\text{-}GABA}$ = 15, $n_{sensory\text{-}Gly}$ = 7; $n_{motor\text{-}Glu}$ = 75, $n_{motor\text{-}GABA}$ = 18, $n_{motor\text{-}Gly}$ = 13),
339 in which the Glu type was predominant (Fig. 4h). Furthermore, along the left-right axis, I type
340 of sensory-related inputs relatively preferred to distal dendritic areas in comparison with I
341 type of motor-related inputs ($P < 0.05$, Two-sample Kolmogorov-Smirnov test), while E type
342 of motor-related inputs biased to proximal dendritic areas in comparison with E type of
343 sensory-related inputs ($P < 0.001$) (Fig. 4i-k), accounting for the differential spatial
344 distributions of sensory- and motor-related synaptic inputs (see Fig. 4e).

345 Interestingly, among the 374 PNs of the LC-NE neuron #3, 69 of them targeted another
346 neurons within the five APEX2-labeled LC-NE neurons, serving as common presynaptic
347 neurons (CPNs) within the LC-NE system ("intra-CPN"). Intra-CPNs were also extensively
348 distributed across sensory-/sensory relay- and motor-related regions (Fig. 4l,m, and
349 Supplementary Video 7). They displayed diverse innervation numbers, with the majority
350 innervating 2 LC-NE neurons (Fig. 4n). Among intra-CPNs with identified E/I properties, the
351 majority were Glu neurons (Fig. 4o). To investigate whether intra-CPNs randomly innervate
352 targeted neurons, we used identical cell numbers and matched innervation number
353 distributions to perform theoretical simulation, revealing that the LC-NE neuron #2 shows
354 higher co-innervation frequency with #3 than other LC-NE neurons (Fig. 4p,q, $P < 0.05$,
355 Chi-square goodness-of-fit test). These results suggest the potential existence of LC-NE
356 subpopulations with preferential co-innervation tendencies. These intra-CPNs may function as
357 a neural substrate underlying synchronous activities observed in LC-NE neuronal
358 populations[48,63,64], serving to coordinate functional outputs of the LC system. Besides, 305 out
359 of the 374 (81.28%) reconstructed PNs of the LC-NE neuron #3 did not target other four
360 LC-NE neurons, and accounted for 330 out of 418 (78.95%) type-identified input synapses of
361 this neuron. In addition, we also observed that the two reconstructed Hcrt neurons only
362 innervated the LC-NE neuron #4 (Extended Data Fig. 11). Collectively, these results indicate
363 that individual LC-NE neurons receive both distinct and common synaptic inputs, aligning
364 with recent findings that endorse the heterogeneous and modular organization of the LC-NE
365 system[48,65-68].

366 Furthermore, among the 374 PNs of the LC-NE neuron #3, we also identified 26 CPNs
367 across different monoaminergic systems ("inter-CPNs", Fig. 4r,s and Supplementary Video 7).
368 Besides targeting the LC-NE neuron #3, these inter-CPNs co-innervated PT-DA or RN-5HT
369 neurons. We conducted *in vivo* calcium imaging on these monoaminergic nuclei
370 simultaneously and found that LC-NE neurons exhibited spontaneous activities synchronized
371 with PT-DA but not RN-5HT neurons (Fig. 4t). The analysis of E/I identities via morphology
372 comparison showed that inter-CPNs between LC-NE and PT-DA neurons predominantly
373 exhibited glutamatergic characteristics (Glu, 5/8; E/I-ambiguous, 3/8), whereas inter-CPNs
374 between LC-NE and RN-5HT neurons were inclined to exhibit a higher ratio of inhibitory
375 ones (Glu, 5/18; GABA, 4/18; Gly, 2/18; E/I-ambiguous, 7/18) (Fig. 4u,v). We hypothesized

that LC-NE and PT-DA neurons might receive shared feedforward driving signals, whereas LC-NE and RN-5HT neurons could be subject to common inhibitory inputs. These inter-CPNs may constitute the structural basis for coordinated activity across distinct monoaminergic systems, enabling more diversified regulation. Interestingly, synaptic inputs originating from both intra- and inter-CPNs preferentially targeted proximal dendritic regions, whereas those from non-CPN sources exhibited a more dispersed spatial innervation (Fig. 4w).

Taken together, these results provide a multi-dimensional view of how synaptic inputs are spatially organized on LC-NE neuronal dendrites: 1) extensive brain-wide convergence; 2) a modality-related distribution of sensory- and motor-related inputs; 3) a strength gradient increasing from distal-to-proximal dendrites; 4) different spatial preferences for E and I inputs; 5) shared innervation within the LC-NE system and across LC-NE, DA and 5HT systems; 6) a proximal dendritic bias of shared innervation (Fig. 4x).

Discussion

In this study, we present a synapse-level, multiplexed molecular annotated ssEM dataset of larval zebrafish. The dataset extends beyond the brain to include the retina, optic nerve, and SC, providing a unique resource for investigating sensorimotor transformation, especially for reconstructing the entire visual pathway. This is particularly valuable considering the zebrafish as a visually dominant species, where the number of cells in a single retina is around two-fifth (70,910/176,810) that of the entire brain. In addition, the ATUM-SEM approach has preserved all sections, allowing for future acquisition of currently unmapped extracerebral structures to expand this resource. While automated reconstruction of the brain has been completed, extensive manual proofreading remains essential to achieve a fully validated whole-brain connectome. This process depends on continuous improvement in online collaborative proofreading systems[69-72]. Besides, this dataset provides a rich APEX2-labeled resource with diverse NM types and a wide range of staining intensities, enabling further optimization of semi-automated or automated reconstruction algorithms for GETEM-labeled cells, particularly those with cytoplasmic labeling[43]. Furthermore, advancing technologies will enable dataset re-alignment and re-segmentation, thereby enhancing the efficiency of connectome validation. In general, we have established a feasible pipeline for molecular annotated whole-brain EM-reconstruction in larval zebrafish, an ideal vertebrate model with the tractable size compared to mammalian connectomes[73].

Fish-X represents the first successful implementation of multiplexed APEX2 labeling in an intact vertebrate brain, simultaneously providing accompanying genetic materials that include both stable zebrafish lines and plasmid constructs. To overcome potential side-effects introduced by the use of H_2O_2 required for the APEX2-DAB reaction[74], we optimized the procedure, including real-time quality control with targeted re-imaging, image repair, image denoising, and multiple rounds of manual verification. Fish-X provides readily identifiable

415 and reliable EM-visible markers, based on which we have extracted structural signatures of
416 corresponding NM neuronal types. Recent studies have demonstrated that local structural
417 features, including perisomatic and synaptic characteristics, enable precise cell type
418 identification[36,37]. The structural signatures we provide can therefore not only facilitate
419 complementary identification of unlabeled cells within Fish-X, but also enable broader
420 application to other zebrafish EM datasets. Recent studies have alternatively utilized CLEM
421 approach, a method in which distinct neuronal populations were fluorescently labeled and
422 subsequently correlated with EM datasets, to achieve neuron-type-specific information
423 transfer from LM to EM datasets[6,10,22,25,34]. This approach directly leverages existing zebrafish
424 transgenic lines and typically yields high-quality images, as H_2O_2 is not required for sample
425 preparation. In comparison, the GETEM strategy exemplified by APEX2 offers distinct
426 advantages: (i) identifiability without complex registration calculations, (ii) multiplexed
427 molecular annotation through orthogonal multi-compartment labeling that overcomes the
428 spectral constraints of fluorescent proteins, and (iii) suitability for long-range projecting axon
429 labeling in local EM reconstructions where complete neuronal morphologies are unavailable.
430 More importantly, the two strategies described above can be combined — the fluorescent
431 signals from APEX2-fused proteins correspond precisely to the corresponding DAB products,
432 serving as matching landmarks that simplify CLEM registration. Moreover, the mesoscopic
433 atlas-based neuronal type identification strategy we proposed is essentially a type of CLEM
434 approach[75]. The mesoscopic atlases enables more cost-effective acquisition of whole-brain
435 projection profiles of more neuronal types[20]. Collectively, these complementary strategies
436 enable comprehensive annotation of zebrafish EM connectomes.

437 While the NM system's regulation of neural networks has been extensively studied, the
438 origins of its upstream inputs and the mechanisms of synaptic integration remain elusive.
439 Investigating the spatial organization of these inputs at a synapse level will enhance our
440 understanding of firing pattern generation[45,46,62]. Our study investigate this issue through the
441 lens of the LC-NE system, an evolutionarily conserved hub regulating brain-wide neural
442 activity and behavioral performance. By comprehensively reconstructing presynaptic inputs
443 onto a single LC-NE neuron, we discovered that individual LC-NE neurons integrate
444 brain-wide inputs with modality-specific spatial organization: inhibitory sensory-related
445 inputs preferentially target distal dendrites, while excitatory motor-related inputs prefer to
446 innervate proximal dendrites. The two modality-related inputs exhibit comparable synaptic
447 strength, with an increasing gradient from distal-to-proximal dendrites. Inspired by the
448 observation in cortical pyramidal neurons, whose somatic activity was markedly reduced
449 when information flow from distal apical dendrites to the soma was blocked during
450 anesthesia[76], we postulate a comparable mechanism in LC-NE neurons — their activity
451 strongly correlates with proximal motor inputs, while sensory-related distal inputs may
452 modulate the excitability of proximal somatodendritic areas and further affect motor-related
453 input-evoked activities, enabling context-dependent modulation.

Besides, the LC-NE system receives convergent inputs and broadcasts signals across the brain, while accumulating evidence reveals its modular functional organization[48,65-68]. The relative prevalence of intra-CPNs targeting 2 – 3 LC-NE neurons provides synapse-level evidence for the functional modularity of the LC-NE system. Intra-CPNs with varying innervation numbers could recruit different numbers or combinations of LC-NE neurons, to generate intensity- and region-distinct NE release, especially given the heterogeneous axonal projections of individual LC-NE neurons[48]. Besides, It is of interest to investigate in the future whether this CPN-based one-to-many *versus* non-CPN-based one-to-one dichotomy corresponds to phasic *versus* tonic firing patterns, transmitting distinct presynaptic information[77,78]. Furthermore, shared innervation across NE, DA and 5HT systems suggests coordinated interactions between distinct NM systems, which may generate diverse spatiotemporal release patterns involving multi-neuromodulator release during different brain states[15-18]. This multiplexed NM-type-annotated EM dataset offers a foundational resource for delineating the input – output organization of multiple NM systems, thereby enabling the elucidation of the synaptic architecture of NM pathways, as well as sensorimotor pathways, within a vertebrate brain.

References

1. White, J. G., Southgate, E., Thomson, J. N. & Brenner, S. The structure of the nervous system of the nematode Caenorhabditis elegans. *Philos. Trans. R. Soc. Lond. B Biol. Sci.* **314**, 1-340 (1986).
2. Hildebrand, D. G. C. et al. Whole-brain serial-section electron microscopy in larval zebrafish. *Nature* **545**, 345-349 (2017).
3. Zheng, Z.-H., et al. A complete electron microscopy volume of the brain of adult drosophila melanogaster. *Cell* **174**, 730-743.e22 (2018).
4. Cook S. J. et al. Whole-animal connectomes of both Caenorhabditis elegans sexes. *Nature* **571**, 63-71 (2019).
5. Scheffer, L. K. et al. A connectome and analysis of the adult Drosophila central brain. *Elife* **9**, e57443 (2020).
6. Svara, F. et al. Automated synapse-level reconstruction of neural circuits in the larval zebrafish brain. *Nat. Methods* **19**, 1357-1366 (2022).
7. Winding, M. et al. The connectome of an insect brain. *Science* **379**, eadd9330 (2023).
8. Dorkenwald, S. et al. Neuronal wiring diagram of an adult brain. *Nature* **634**, 124-138 (2024).
9. Shapson-Coe, A. et al. A petavoxel fragment of human cerebral cortex reconstructed at nanoscale resolution. *Science* **384**, eadk4858 (2024).
10. MICrONS Consortium. Functional connectomics spanning multiple areas of mouse visual cortex. *Nature* **640**, 435-447 (2025).
11. Zhang, Q.-Y., Lee, W. A., Paul, D. L. & Ginty, D. D. Multiplexed peroxidase-based electron microscopy labeling enables simultaneous visualization of multiple cell types. *Nat. Neurosci.* **22**, 828-839 (2019).
12. Ngai, J. BRAIN 2.0: Transforming neuroscience. *Cell* **185**, 4-8 (2022).

13. Gamlin, C.R. et al. Connectomics of predicted Sst transcriptomic types in mouse visual cortex. *Nature* **640**, 497-505 (2025).
14. Schneider-Mizell C.M. et al. Inhibitory specificity from a connectomic census of mouse visual cortex. *Nature* **640**, 448-458 (2025).
15. Marder, E. Neuromodulation of neuronal circuits: back to the future. *Neuron* **76**, 1-11 (2012).
16. McCormick, D. A., Nestvogel, D. B. & He, B.-J. Neuromodulation of brain state and behavior. *Annu. Rev. Neurosci.* **43**, 391-415 (2020).
17. Mei, J., Muller, E. & Ramaswamy, S. Informing deep neural networks by multiscale principles of neuromodulatory systems. *Trends Neurosci.* **45**, 237-250 (2022).
18. Li, F.-N., Zhang, C.-M. & Du, J.-L. Neuromodulatory processing in the bi-pathway brain architecture. *Curr. Opin. Neurobiol.* **93**, 103055 (2025).
19. Lam, S. S. et al. Directed evolution of APEX2 for electron microscopy and proximity labeling. *Nat. Methods* **12**, 51-54 (2015).
20. Du, X.-F. et al. Central nervous system atlas of larval zebrafish constructed using the morphology of single excitatory and inhibitory neurons. *bioRxiv* doi:10.1101/2025.06.06.658008 (2025).
21. Wang, Y.-F. et al. BrAVe: a unified framework for 3D interactive and integrative exploration and analysis of cross-modal brain atlas data. ***Co-submitted to Nature.***
22. Wanner, A. A. & Friedrich, R. W. Whitening of odor representations by the wiring diagram of the olfactory bulb. *Nat. Neurosci.* **23**, 433-442 (2020).
23. Friedrich, R. W. & Wanner, A. A. Dense circuit reconstruction to understand neuronal computation: focus on zebrafish. *Annu. Rev. Neurosci.* **44**, 275-293 (2021).
24. Brittin, C. A., Cook, S. J., Hall, D. H., Emmons, S. W. & Cohen, N. A multi-scale brain map derived from whole-brain volumetric reconstructions. *Nature* **591**, 105-110 (2021).
25. Boulanger-Weill, J. et al. Correlative light and electron microscopy reveals the fine circuit structure underlying evidence accumulation in larval zebrafish. *bioRxiv* doi:10.1101/2025.03.14.643363 (2025).
26. Kasthuri, N. et al. Saturated reconstruction of a volume of neocortex. *Cell* **162**, 648-661 (2015).
27. Motta, A. et al. Dense connectomic reconstruction in layer 4 of the somatosensory cortex. *Science* **366**, eaay3134 (2019).
28. Gour, A. et al. Postnatal connectomic development of inhibition in mouse barrel cortex. *Science* **371**, eabb4534 (2021).
29. Loomba, S. et al. Connectomic comparison of mouse and human cortex. *Science* **377**, eabo0924 (2022).
30. Ding, Z.-K. et al. Functional connectomics reveals general wiring rule in mouse visual cortex. *Nature* **640**, 459-469 (2025).
31. Wanner, A. A., Genoud, C., Masudi, T., Siksou, L. & Friedrich, R. W. Dense EM-based reconstruction of the interglomerular projectome in the zebrafish olfactory bulb. *Nat. Neurosci.* **19**, 816-825 (2016).
32. Vishwanathan, A. et al. Electron microscopic reconstruction of functionally identified cells in a neural integrator. *Curr. Biol.* **27**, 2137-2147.e3 (2017).
33. Vishwanathan, A. et al. Predicting modular functions and neural coding of behavior from

a synaptic wiring diagram. *Nat. Neurosci.* **27**, 2443-2454 (2024).
34. Petkova, M. D. et al. A connectomic resource for neural cataloguing and circuit dissection of the larval zebrafish brain. *bioRxiv* doi:10.1101/2025.06.10.658982 (2025).
35. Tavakoli, M. R. et al. Light-microscopy-based connectomic reconstruction of mammalian brain tissue. *Nature* **642**, 398-410 (2025).
36. Eckstein, N. et al. Neurotransmitter classification from electron microscopy images at synaptic sites in Drosophila melanogaster. *Cell* **187**, 2574-2594.e23 (2024).
37. Elabbady, L. et al. Perisomatic ultrastructure efficiently classifies cells in mouse cortex. *Nature* **640**, 478-486 (2025).
38. Atasoy, D. et al. A genetically specified connectomics approach applied to long-range feeding regulatory circuits. *Nat. Neurosci.* **17**, 1830-1839 (2014).
39. Shigemoto, R. & Joesch, M. The genetic encoded toolbox for electron microscopy and connectomics. *Wiley Interdiscip. Rev. Dev. Biol.* **6** (2017).
40. Cruz-Lopez, D., Ramos, D., Castilloveitia, G. & Schikorski, T. Quintuple labeling in the electron microscope with genetically encoded enhanced horseradish peroxidase. *PLoS One* **13**, e0200693 (2018).
41. Jiang, Z.-D. et al. Genetically encoded tags for direct synthesis of EM-visible gold nanoparticles in cells. *Nat. Methods* **17**, 937-946 (2020).
42. Böhm, U. L. et al. CSF-contacting neurons regulate locomotion by relaying mechanical stimuli to spinal circuits. *Nat. Commun.* **7**, 10866 (2016).
43. Joesch, M. et al. Reconstruction of genetically identified neurons imaged by serial-section electron microscopy. *Elife* **5**, e15015 (2016).
44. Tay, T. L., Ronneberger, O., Ryu, S., Nitschke, R. & Driever, W. Comprehensive catecholaminergic projectome analysis reveals single-neuron integration of zebrafish ascending and descending dopaminergic systems. *Nat. Commun.* **2**, 171 (2011).
45. Schwarz, L. A. et al. Viral-genetic tracing of the input-output organization of a central noradrenaline circuit. *Nature* **524**, 88-92 (2015).
46. Schwarz, L. A. & Luo, L.-Q. Organization of the locus coeruleus-norepinephrine system. *Curr. Biol.* **25**, R1051-R1056 (2015).
47. Rho, H. J., Kim, J. H. & Lee, S. H. Function of selective neuromodulatory projections in the mammalian cerebral cortex: comparison between cholinergic and noradrenergic systems. *Front. Neural Circuits* **12**, 47 (2018).
48. Zhang, C.-M. et al. Multiple-level organizational logic of the locus coeruleus-norepinephrine system in structure and function. *bioRxiv* doi:10.1101/2025.06.11.659024 (2025).
49. Shang, C.-F., Wang, Y.-F. & Du, J.-L. Information integration for motor generation. *Curr. Opin. Physiol.* **8**, 116-120 (2019).
50. Witvliet, D. et al. Connectomes across development reveal principles of brain maturation. *Nature* **596**, 257-261 (2021).
51. Usher, M., Cohen, J. D., Servan-Schreiber, D., Rajkowski, J. & Aston-Jones, G. The role of locus coeruleus in the regulation of cognitive performance. *Science* **283**, 549-554 (1999).
52. Berridge, C. W. & Waterhouse, B. D. The locus coeruleus-noradrenergic system: modulation of behavioral state and state-dependent cognitive processes. *Brain Res. Brain*

Res. Rev. **42**, 33-84 (2003).
53. Aston-Jones, G. & Cohen, J. D. An integrative theory of locus coeruleus-norepinephrine function: adaptive gain and optimal performance. *Annu. Rev. Neurosci.* **28**, 403-450 (2005).
54. Bouret, S. & Sara, S. J. Network reset: a simplified overarching theory of locus coeruleus noradrenaline function. *Trends Neurosci.* **28**, 574-582 (2005).
55. Sara, S. J. The locus coeruleus and noradrenergic modulation of cognition. *Nat. Rev. Neurosci.* **10**, 211-223 (2009).
56. Totah, N. K., Neves, R. M., Panzeri, S., Logothetis, N. K. & Eschenko, O. The locus coeruleus is a complex and differentiated neuromodulatory system. *Neuron* **99**, 1055-1068.e6 (2018).
57. Foote, S. L. & Berridge, C. W. New developments and future directions in understanding locus coeruleus - Norepinephrine (LC-NE) function. *Brain Res.* **1709**, 81-84 (2019).
58. Poe, G. R. et al. Locus coeruleus: a new look at the blue spot. *Nat. Rev. Neurosci.* **21**, 644-659 (2020).
59. Vohra, S. K. et al. Fishexplorer: A multimodal cellular atlas platform for neuronal circuit dissection in larval zebrafish. *bioRxiv* doi:10.1101/2025.07.14.664689 (2025).
60. Hayworth, K. J. et al. Imaging ATUM ultrathin section libraries with WaferMapper: a multi-scale approach to EM reconstruction of neural circuits. *Front. Neural Circuits* **8**, 68 (2014).
61. Tao, C.-L. et al. Differentiation and characterization of excitatory and inhibitory synapses by cryo-electron tomography and correlative microscopy. *J. Neurosci.* **38**, 1493-1510 (2018).
62. Tian, J. et al. Distributed and mixed information in monosynaptic inputs to dopamine neurons. *Neuron* **91**, 1374-1389 (2016).
63. Christie, M. J., Williams, J. T. & North R. A. Electrical coupling synchronizes subthreshold activity in locus coeruleus neurons in vitro from neonatal rats. *J. Neurosci.* **9**, 3584-3589 (1989).
64. Ishimatsu, M. & Williams, J. T. Synchronous activity in locus coeruleus results from dendritic interactions in pericoerulear regions. *J. Neurosci.* **16**, 5196-5204 (1996).
65. Chandler, D. J., Gao, W.-J. & Waterhouse, B. D. Heterogeneous organization of the locus coeruleus projections to prefrontal and motor cortices. *Proc. Natl. Acad. Sci. U. S. A.* **111**, 6816-6821 (2014).
66. Uematsu, A. et al. Modular organization of the brainstem noradrenaline system coordinates opposing learning states. *Nat. Neurosci.* **20**, 1602-1611 (2017).
67. Hirschberg, S., Li, Y., Randall, A., Kremer, E. J. & Pickering, A. E. Functional dichotomy in spinal- vs prefrontal-projecting locus coeruleus modules splits descending noradrenergic analgesia from ascending aversion and anxiety in rats. *Elife* **6**, e29808 (2017).
68. Chandler, D. J. et al. Redefining noradrenergic neuromodulation of behavior: impacts of a modular locus coeruleus architecture. *J. Neurosci.* **39**, 8239-8249 (2019).
69. Dorkenwald, S. et al. FlyWire: online community for whole-brain connectomics. *Nat. Methods* **19**, 119-128 (2022).
70. Schmidt, M., Motta, A., Sievers, M. & Helmstaedter, M. RoboEM: automated 3D flight

628 tracing for synaptic-resolution connectomics. *Nat. Methods* **21**, 908-913 (2024).
629 71. Celii, B. et al. NEURD offers automated proofreading and feature extraction for
630 connectomics. *Nature* **640**, 487-496 (2025).
631 72. Dorkenwald, S. et al. CAVE: Connectome Annotation Versioning Engine. *Nat. Methods*
632 **22**, 1112-1120 (2025).
633 73. Abbott, L. F. et al. The mind of a mouse. *Cell* **182**, 1372-1376 (2020).
634 74. Lee, S.Y. et al. Directed evolution of LaccID for cell surface proximity labeling and
635 electron microscopy. *Nat. Chem. Biol.* Online ahead of print (2025).
636 75. Costa, M., Manton, J. D., Ostrovsky, A. D., Prohaska, S. & Jefferis, G. S. NBLAST:
637 rapid, sensitive comparison of neuronal structure and construction of neuron family
638 databases. *Neuron* **91**, 293-311 (2016).
639 76. Suzuki, M. & Larkum, M. E. General anesthesia decouples cortical pyramidal neurons.
640 *Cell* **180**, 666-676.e13 (2020).
641 77. Ghosh, S. & Maunsell, J. H. R. Locus coeruleus norepinephrine contributes to
642 visual-spatial attention by selectively enhancing perceptual sensitivity. *Neuron* **112**,
643 2231-2240.e5 (2024).
644 78. Grimm, C. et al. Tonic and burst-like locus coeruleus stimulation distinctly shift network
645 activity across the cortical hierarchy. *Nat. Neurosci.* **27**, 2167-2177 (2024).
646

Methods

Zebrafish husbandry

Adult Zebrafish (*Danio rerio)* were kept in a circulating system at 28℃ under a 14:10 hour light-dark cycle. All animal protocols were reviewed and approved by the Animal Care and Use Committee of the Center for Excellence in Brain Science and Intelligence Technology (CEBSIT), Chinese Academy of Sciences (NA-046-2023). Larvae were fed with *Brachionid* rotifers from 4.5 – 9.0 dpf, then switched to freshly hatched *Artemia* nauplii thereafter. The sex of embryonic and larval zebrafish was undetermined.

Zebrafish lines

All transgenic zebrafish larvae were in *nacre* background. The *vmat2*, *th1*, *dbh*, *tph2*, *hcrt*, *glyt2*, *vglut2a*, *gad1b* promoters were used to label NE/DA/5HT, NE/DA, NE, 5HT, Hcrt, Gly, Glu, and GABA neurons, respectively. Published fish lines used in this study include *Tg(slc6a5:GFP)cf3* (*abbreviation*: *Tg(glyt2:GFP)*)[79], *Tg(-2.0Fru.Hcrt:EGFP)zf11* (*Tg(Hcrt:EGFP)*)[80], *Tg(5×UAS:EGFP)nkuasgfp1a* (*Tg(5×UAS-TATA:EGFP)*)[81], *Tg(elavl3:Hsa.H2B-GCaMP6f)jf7* (*Tg(HuC:H2B-GCaMP6f)*)[82], *Tg(5×UAS-hsp70l:GCaMP6s)nkUAShspzGCaMP6s13a* (*Tg(UAS:GCaMP6s)*)[83], *Ki1(th:EGFP)ion27d* (*Ki1(th:EGFP)*)[84], *Ki(th:GAL4-VP16)ion32d* (*Ki(th:GAL4-VP16)*)[84], *Ki(tph2:EGFP)ion39d* (*Ki(tph2:EGFP)*)[84], *Tg(slc17a6:GAL4FF)ion177d* (*Tg(vglut2a:GAL4FF)*)[85]. The followings are unpublished fish lines. *TgBAC(gad1b:GAL4-VP16)ion19h*[20] was provided by Dr. Jie He and *gSAIzGFFM242A* (*Gt(vmat2:GAL4FF)*) was provided by Dr. Koichi Kawakami. *Ki(tph2:GAL4FF,myl7:EGFP)ion127d* (*Ki(tph2:GAL4FF,cmlc2:EGFP)*) was constructed using a CRISPR/Cas9-based knockin method[84]. *Tg(dbh:GAL4FF;5×UAS-hsp:cytosol-APEX2-TagRFP)ion142d* (*Tg(dbh:GAL4FF;UAS:cytosol-APEX2-TagRFP)*), *Tg(hcrt:APEX2-TagRFP-NLS)ion100d* (*Tg(hcrt:APEX2-TagRFP-NLS)*), and *Tg(slc6a5:Hsa.Cox8a-APEX2-TagRFP)ion97d* (*Tg(glyt2:MITO-APEX2-TagRFP)*) were constructed using the Tol2-based transgenic system[86]. The *APEX2* sequence was cloned from the commercial plasmid *Bact2-APEX2-GBP*[87] (Addgene, Cat# 67668). The *dbh*, *hcrt*, and *glyt2* promoter sequences were cloned from plasmids *pTol2-dbh (short)-GAL4FF-5XUAS-hsp-TRPV1-RFPT*, *pTol2-hcrt-GAL4-VP16*, and *pTol2-glyt2-P2A-ECFP*, respectively. In addition, we generated the plasmid *pTol2-5×UAS-2×Cox8a-APEX2-TagRFP* to specifically label mitochondria in Glu and GABA neurons by crossing with E/I specific GAL4 reporter lines. Signal peptide sequences below were used to target distinct subcellular compartments.

Three tandem nuclear localization sequence (*3×NLS*):
TACCTTTCTCTTCTTTTTTGGATCTACCTTTCTCTTCTTTTTTGGATCTACCTTTCTCT
TCTTTTTTGG

Two tandem cytochrome c oxidase subunit 8A (*MITO*; labeled as *2×Cox8a* in plasmid):

ATGTCCGTCCTGACGCCGCTGCTGCTGCGGGGCTTGACAGGCTCGGCCCGGCGGC
TCCCAGTGCCGCGCGCCAAGATCCATTCGTTGGGGGATCTGTCCGTCCTGACGCCG
CTGCTGCTGCGGGGCTTGACAGGCTCGGCCCGGCGGCTCCCAGTGCCGCGCGCCA
AGATCCATTCGTTG

Immunostaining

Larvae were fixed overnight on a shaker at 4℃ using 4% paraformaldehyde (PFA, Sigma, Cat# 158127) prepared in phosphate-buffered saline (PBS). Following three 5-min washes with PBS containing 1% Tween-20 (PBST), brains were carefully dissected using fine forceps and subjected to another three PBST washes. Samples then underwent graded dehydration and rehydration through sequential incubation in (v/v): 25% methanol/75% PBST (5 min, RT), 50% methanol/50% PBST (5 min, RT), 75% methanol/25% PBST (5 min, RT), 100% methanol (4 h, -20℃), followed by reverse gradient to 25% methanol, then three 5-min PBST washes at RT. After ddH_2O rinse (5 min, RT) and acetone treatment (10 min, -20℃), samples were rehydrated through ddH_2O and three final PBST washes. Blocking was performed overnight at 4℃ with gentle shaking, followed by incubation with primary antibodies (1:200 in blocking buffer) at 4℃ for 24 – 48 h. After primary antibody recovery and three quick PBST rinses, extended washing was performed (2 × 1 h, 1 × 20 min, 1 × 10 min). Secondary antibodies (1:500 in blocking buffer) were applied at 4℃ for 36 h, followed by removal, three quick PBST washes, and final rinses (3 × 10 min, 1 × 30 min) before light-protected storage on ice for fluorescence imaging. Commercial antibodies included Anti-Orexin-A antibody (Millipore, Cat# AB3704), Anti-Tyrosine Hydroxylase antibody (Millipore, Cat# MAB318), Alexa Fluor® 488 Goat anti-Rabbit secondary antibody (Abcam, Cat# AB150077), and Alexa Fluor® 568 Goat anti-Mouse secondary antibody (Invitrogen, Cat# A-11004).

***In vivo* structural and functional imaging**

At 3 dpf, multiplexed APEX2-labeled larvae were initially screened using an upright fluorescence stereomicroscope. The preparations, embedded in 1.5% low-melting-point agarose (Invitrogen, Cat# 15517014), were carefully verified at 5 dpf using an upright fluorescence microscope. The labeling efficiency was evaluated to determine larvae were used for further EM sample preparation. At 6 dpf, larvae were paralyzed with 1 mg/mL α-bungarotoxin (Tocris, Cat# 2133) and dorsally embedded in 1.5% low-melting-point agarose. Morphological fluorescence imaging was performed using an upright confocal laser scanning microscope (FV3000, Olympus, Japan) equipped with a 40× water-immersion objective (NA = 0.8). Imaging parameters included a frame size of 635.9 × 635.9 μm^2 (0.621 × 0.621 μm^2 per pixel), with two-field stitching along the rostrocaudal axis to cover the SC, Z-axis intervals of 1 – 1.5 μm, and 2 – 3 line averaging. Selected brain regions were further imaged at higher zoom factors to resolve fine spatial patterns of APEX2 signals.

To simultaneously record calcium dynamics in LC-NE, PT-DA, and RN-5HT neurons, we performed *in vivo* calcium imaging on 6-dpf

723 *Ki(th:GAL4-VP16);Ki(tph2:GAL4FF,cmlc2:EGFP);Tg(UAS:GCaMP6s)* larvae, using a
724 confocal microscope (FV3000, Olympus, Japan). Imaging parameters included a frame size
725 of 636.4 × 636.4 μm² (1.243 × 1.243 μm^2 per pixel), with resonant scanning mode, imaging
726 depth of ~200 μm, Z-axis intervals of 10 μm, volumetric imaging rate at ~0.72 Hz, and total
727 acquisition duration of ~30 min per session.

728 **DAB staining**

729 The optimized DAB staining protocol was adapted from published procedures[88]. The 0.1 M
730 Tris-HCl buffer (pH 7.4) was prepared by dissolving 0.6055 g Tris-Base (Millipore, Cat#
731 648311) in 50 mL of ultrapure water, with pH adjustment using concentrated HCl. A 10 mg
732 tablet of 3,3'-diaminobenzidine tetrahydrochloride (DAB·4HCl, Sigma, Cat# D5905) was
733 subsequently dissolved in 10 mL of this buffer through vigorous vortexing under
734 light-protected conditions. The solution was then filtered through a 0.22-μm filter (Millipore,
735 Millex™-GP 0.22-μm filter) to obtain a 1 mg/mL DAB stock solution, which was stored at
736 4℃ and protected from light. Samples were sequentially rinsed with 0.1 M phosphate buffer
737 (3 × 10 min), Tris-HCl buffer (2 × 10 min), and DAB solution (2 × 10 min) on a shaker at 4℃
738 to remove residual aldehydes. For the reaction, 1 μL of 30% H_2O_2 (Sinopharm Chemical
739 Reagent Co., Ltd., Cat# 10011218) was mixed with 1 mL DAB stock to prepare the working
740 solution, and then samples were incubated for 2 h at RT in complete darkness. The reaction
741 was terminated by washing with Tris-HCl buffer (2 × 10 min). The catalysis by APEX2 of
742 DAB polymerization resulted in dark brown precipitates, which were clearly visible under
743 bright-field stereomicroscope. Post-fixation with osmium tetroxide (OsO_4) was conducted
744 immediately following DAB staining to preserve the osmiophilic reaction products.

745 **EM sample preparation**

746 A mixed fixative containing 2% PFA and 2% glutaraldehyde (GA) was used for effective
747 whole-brain fixation. A 1 mL aliquot of 25% GA (Sigma, Cat# G5882, stored at -20℃) was
748 thawed at 4℃ under light protection. Concurrently, 1 g PFA powder was dissolved in 20 mL
749 of ultrapure water within a fume hood, with 1 – 2 drops of 1 M NaOH added. The solution
750 was then sealed, protected from light, and heated at 65℃ with magnetic stirring until fully
751 clarified. After cooling to RT, the solution was filtered through a 0.22 μm filter to yield 5%
752 PFA stock. The 10-mL working fixative was prepared immediately before dissection by
753 mixing 4 mL of 5% PFA, 0.8 mL of 25% GA, 5 mL of 0.1 M phosphate buffer (pH 7.4), and
754 0.2 mL of ultrapure water. Larvae were embedded in 1.5% low-melting-point agarose
755 dissolved in extracellular solution (in mM: 134 NaCl, 2.9 KCl, 2.1 $CaCl_2 \cdot 2H_2O$, 1.2
756 $MgCl_2 \cdot 6H_2O$, 10 HEPES, 10 glucose; 290 mOsm, pH 7.8). The agarose covering dorsal
757 epidermis and pectoral fins was removed. Using glass micropipettes, the skin was carefully
758 dissected from the hindbrain ventricle while avoiding damage to tissues. The trunk was
759 rapidly transected anterior to the swim bladder using ophthalmic scissors, after which the
760 head was gently extracted with fine forceps and immediately immersed in fresh fixative.

761 Fixed samples were sealed and stored at 4℃ in darkness overnight.

762 Subsequent procedures were adapted from the rOTO protocol[89,90]. First, a 1:1 (v/v)
763 mixture of 0.2 M phosphate buffer and 2% OsO_4 (TED PELLA, Cat# 18451) was prepared to
764 obtain an OsO_4-phosphate solution, which was then used to prepare a reduced
765 OsO_4-phosphate solution containing 0.03 g/mL potassium hexacyanoferrate trihydrate (Sigma,
766 Cat# P9387). All OsO_4-containing solutions were freshly prepared within a fume hood, tightly
767 sealed, protected from light at 4℃, and properly collected for disposal after use. Fixed
768 samples were washed with 0.1 M phosphate buffer at 4℃ (4 × 10 min) and then immersed in
769 the OsO_4-phosphate solution (200 – 500 μL per 1.5 mL tube, 2 h, 4℃). Concurrently, a 0.01
770 g/mL aqueous thiocarbohydrazide (TCH, Sigma, Cat# 88535) solution was placed in a 60℃
771 oven and gently flipped to facilitate dissolution. The TCH solution was removed from the
772 oven and allowed to cool slightly above RT before use. The solution was then filtered through
773 a 0.22 μm filter directly into the sample tube that had been rinsed with ultrapure water (3 × 10
774 min, 4℃; 1 × 10 min, RT). After a 30-min light-protected TCH treatment at RT, samples were
775 washed with ultrapure water (4 × 10 min, 4℃). The reduced OsO_4-phosphate solution was
776 then added (200 – 500 μL per 1.5 mL tube, 30 min, RT). Afterward, samples were washed
777 with ultrapure water (4 × 10 min, 4℃). Meanwhile, a 2% aqueous uranyl acetate solution
778 (EMS, Cat# 22400) was centrifuged at 13,000 rpm, and the supernatant was carefully
779 transferred into the sample tube (200 μL per 1.5 mL tube). Samples were then sealed and
780 stored at 4℃ overnight, protected from light.

781 On the next day, the uranyl acetate waste solution was collected for proper disposal,
782 followed by washing samples with ultrapure water (3 × 10 min). Subsequently, a graded
783 dehydration series was performed on ice using ethanol solutions (30%, 50%, 70%, 80%, 90%,
784 95%, and 100% v/v, each for 10 min) followed by anhydrous acetone (2 × 10 min). On the
785 day of fixation, the resin volume was calculated, and the premix was prepared by sequentially
786 pipetting 10 mL of Pon-812 epoxy resin monomer (SPI, Cat# 90529-77-4), 3.36 mL of
787 dodecenyl succinic anhydride (DDSA, SPI, Cat# 26544-38-7), and 7.04 mL of nadic methyl
788 anhydride (NMA, SPI, Cat# 25134-21-8) into a pre-dried tube at RT to form a
789 three-component premix. This was then sealed and mixed on a rotary mixer for at least 3
790 hours. Resin infiltration was conducted immediately following dehydration. 400 μL DMP-30
791 epoxy accelerator (SPI, Cat# 90-72-2) was added to 20 mL premix, followed by 30-min rotary
792 mixing to prepare the final resin solution. The resin solution was either used immediately
793 after a 30-min bubble-settling period or kept mixing to prevent polymerization at RT. Samples
794 underwent graded acetone-resin infiltration at ratios of 3:1, 1:1, and 1:3 (v/v) for 8 h, 8h, and
795 overnight, respectively. They were then transferred to resin-filled vials, subject to negative
796 pressure using a 5 mL syringe, and placed on a horizontal shaker for resin infiltration.

797 This process was conducted over two days with resin changes occurring twice daily at
798 intervals of 8 – 12 h. All procedures were performed under controlled environmental
799 conditions (temperatures < 25℃; humidity < 30%). Following the two-day resin infiltration,

samples were transferred to pre-dried 21-well flat molds and oriented using sterile toothpicks. The molds were then placed in a drying box containing silica gel beads and polymerized at 37℃ for 8 – 12 h. After verifying and minimally adjusting sample orientation at night, the temperature was first increased to 45℃ overnight, then to 60℃ the following morning. Fully polymerized blocks were removed from the oven after 48 h and stored in a dry cabinet.

X-ray tomography

X-ray tomography was conducted to rapidly and non-destructively evaluate the quality of EM samples using the Xradia 520 Versa system (Zeiss, Germany) at the Instrumental Analysis Center of Shanghai Jiao Tong University. Samples exhibiting uniform staining, minimal deformation, and no apparent mechanical damage were selected for further ultrathin sectioning and SEM imaging. Samples were scanned at 60 kV with 1 μm^3 voxel resolution (~2 h per sample). Data processing was conducted using Dragonfly (Object Research Systems, Canada). Sequential images were imported with resampling parameters and voxel resolution specified. Sample orientation was interactively manipulating reference axes in the display window. Selected views were exported as projection sequences via the "*Derive new from current view*" function. 3D animations were created using the *Video marker* tool. The video denoising was performed using an open-source Real-ESRGAN-General-x4v3 model.

Whole-brain ultrathin section collection

Using an ultramicrotome equipped with an automated tape-collecting system (ATUMtome, RMC, USA), 33-nm serial sections were obtained[2]. Prior to collection, trimmed excess blank resin around the larva using a double-edged razor blade. The front guide slot of the ATUMtome was properly positioned, and parameters including sectioning speed (0.8 mm/s), tape-advancing speed (0.6 mm/s), and water refilling interval (5-sec duration every 8 min) were set. The anti-static device and intermittent water replenishment system were activated to ensure sequential and stable section collection on hydrophilic, conductive polyimide film strips (KAPTON-PET, DuPont, USA). If section instability was observed during collection (e.g., incomplete sections), immediately halted sectioning and either repositioned the knife edge or replaced the diamond knife (UltraMaxi, Diatome, Switzerland). Throughout the process, ambient conditions were maintained at 25℃ and 60% humidity. Following collection, section-bearing strips were segmented and mounted onto 4-inch monocrystalline silicon wafers using 0.8-mm-wide conductive adhesive tape (SPI, USA), with careful pressing to eliminate air bubbles. The mounted wafer was placed into a LEICA EM ACE 600 high-vacuum coater for carbon deposition (6 – 10 nm film thickness). The section surfaces were cleaned using nitrogen gas blowing, and subsequently stored in a dry cabinet at 25℃ and 30% humidity. The entire collection process, which spent three days and utilized three diamond knives, yielded an overall damage rate of 6.56%. Sections were numbered #2594 – #25480 in a caudal-to-rostral order. The damaged 1,503 sections with folds, tears, and severe contamination were algorithmically repaired to ensure that intact portions were registered to

838 adjacent sections[91]. The majority of defects did not occur at identical locations across adjacent
839 sections, thus collectively posing no substantial impact on proofreading.

840 **SEM image acquisition**

841 To enhance sample stability and backscattered electron (BSE) signal contrast, wafers were
842 pre-irradiated using a custom-built irradiation system (9 mA, 2 kV, 10 s continuous exposure).
843 Post-irradiation wafers were transferred to an optical microscope (Clippers FBT, China) for
844 the acquisition of navigation images via line-scan imaging with 7.6 μm pixel resolution.
845 Image acquisition was conducted simultaneously across three SEMs (Navigator
846 NeuroSEM100, FBT, China), each equipped with a custom-built collection software designed
847 to maximize efficiency in image output. The pixel resolution was set to 4 nm, the dwell time
848 to 43.5 ns, and the acceleration voltage to 2 kV. Auto focus and astigmatic correction were
849 configured to 80 s per section. To expedite acquisition efficiency and imaging success rate, a
850 region-specific focusing protocol coupled with photography was implemented. Each section
851 was divided into a grid of ~54 tiles (arranged in 9 rows × 6 columns) at 12,000 × 12,000
852 pixels per tile. The adjacent tiles were acquired with a 12% overlapping area. 16 tiles (4 × 4
853 arrangement) constituted one standard region. Edge regions containing fewer than 16 tiles
854 were processed equivalently. Regions were sequentially numbered and navigated in a
855 serpentine pattern. Prior to high-resolution scanning, a low-resolution focus was conducted to
856 ensure the algorithm efficacy in pinpointing the optimal focal range at the center of the
857 section, which was set at a resolution of 50 nm with a dwell time of 80 ns. The stage was then
858 oriented to the first region's center for high-resolution focusing and astigmatism correction
859 with a resolution of 4 nm and a dwell time of 80 ns, followed by snake-pattern tile acquisition.
860 After capturing all tiles within a region, the stage advanced to the next region (2.5 s/tile for
861 positional adjustment and data transfer). This cycle iterated until full-section coverage was
862 achieved, maintaining serpentine navigation between regions. The process was repeated
863 automatically for subsequent sections until wafer-wide imaging completion.

864 To enhance the accuracy and robustness of large-scale EM image processing, we
865 introduced an image quality assessment and tissue validity detection module prior to
866 algorithmic analysis. A 2D U-Net model was trained to evaluate image sharpness and
867 assigned a quality score to each section. Low-quality images were then reviewed using a
868 custom annotation tool, allowing experts to determine whether re-acquisition or replacement
869 was necessary. Besides, we implemented CNN-based tissue mask generation. A U-Net model
870 was trained on three manually annotated chunks (8,600 × 8,600 × 31 voxels at 32 × 32 ×
871 33 nm^3 per voxel) to classify voxels into brain tissues, backgrounds, and defect regions (e.g.,
872 folds, tears). All predicted masks were manually reviewed. The quality scores and tissue
873 masks were applied throughout the processing pipeline for artifact exclusion and
874 region-of-interest selection, supporting segmentation and agglomeration.

875 **Image stitching and alignment**

The 3D volume registration of EM images was accomplished through tile stitching and section alignment. The stitching workflow proceeded through three computational stages: 1) feature detection and matching using Scale-Invariant Feature Transform (SIFT) descriptors[92] extracted from tile overlap areas; 2) pairwise displacement estimation via coordinate transformation analysis; 3) global position optimization through linear least squares minimization. Specifically, SIFT-matched feature point pairs served as the basis for calculating local translation vectors between tiles. To mitigate error accumulation, a global optimization framework simultaneously adjusted all tile positions by minimizing the total displacement error across the entire section.

A multi-scale alignment method was implemented to register serial sections, first through coarse-scale processing followed by fine-scale refinement. To address error accumulation, the pipeline employed a sub-volume-division strategy, partitioning the original dataset into 764 spatially coherent stacks (each containing 31 consecutive sections). Continuity across stacks was established by selecting the first section of each stack as a reference section (764 total). These references underwent affine transformation to correct notable deformations while maintaining spatial invariance throughout alignment, serving as stable pivots to prevent cumulative error propagation. Alignment then proceeded within each stack, from coarse to fine scales. Sections were downsampled 32-fold during coarse-scale alignment. Correspondences between two adjacent sections were initially extracted using SIFT descriptors and subsequently filtered using the RANSAC algorithm[93]. Affine transformation was applied to align adjacent sections. Sections were downsampled 8-fold during fine-scale alignment. Damaged sections were first aligned to their neighbors using an expected affine method[91]. Subsequently, an optimized elastic method[94] generated dense correspondence fields between adjacent sections, guiding the iterative refinement of deformation meshes that balanced local adaptability with global smoothness. Finally, Thin-Plate Spline (TPS) transformations[95] extrapolated these deformations to original-resolution sections, preserving ultrastructural continuity at synaptic resolution.

Bidirectional CLEM

To match the resolution of the brain template of the Zebrafish Mesoscopic Atlas (1 μm^3 per voxel), the 764 reference sections mentioned above were further downsampled in the xy-plane to generate downsampled whole-brain EM images (992 × 992 × 990 nm^3 per voxel). Multimodal image registration was accomplished through a three-stage approach. First, whole-brain nuclei were extracted from both the Zebrafish Mesoscopic Atlas and the ssEM dataset to create nuclei point clouds, which were then rigidly aligned using the Iterative Closest Point (ICP) algorithm[96]. Manually-annotated nuclei from four 6-dpf *Tg(HuC:H2B-GCaMP6f)* larvae were used to generate the average point cloud for the LM brain template, while nuclei from the ssEM dataset were automatically segmented. Second, the EM images were globally constrained using X-ray tomography data, to correct the

distortion along the rostral-caudal axis ("banana effect"). Third, bidirectional deformation fields between LM and EM spaces were computed through 3D template matching and TPS transformations. Soma regions across the entire brain, along with other EM-identifiable regions including the pineal gland, pituitary gland, and bilateral optic tectal neuropils, were manually annotated on downsampled whole-brain EM images and registered with their counterparts in the brain template of the Zebrafish Mesoscopic Atlas, serving as reference landmarks for joint optimization.

Chunk-based 3D reconstruction

Whole-brain 3D reconstruction was performed through an automated pipeline consisting of: (1) image enhancement and denoising, (2) local registration, (3) dense segmentation, (4) intra-chunk agglomeration, and (5) inter-chunk stitching. To efficiently process large-scale computational tasks, we implemented a distributed computing strategy based on spatial block partitioning. Specifically, the original 3D volume was divided into a series of overlapping chunks to ensure boundary continuity and consistency in prediction. These chunks were then preprocessed and spatially realigned, and subsequently treated as independent inference tasks scheduled for parallel execution. The entire computational workflow was deployed on a high-performance distributed parallel computing architecture managed by the Slurm (Simple Linux Utility for Resource Management) workload manager. All sub-tasks were automatically submitted via batch scripts to a Slurm-managed HPC (High-Performance Computing Cluster) consisting of more than 30 nodes. Based on the availability of computational resources, the scheduler dynamically distributed tasks across multiple physical nodes. Each node was equipped with a heterogeneous configuration of GPUs, including NVIDIA® A100, V100, and GeForce RTX 4090 models, thereby maximizing utilization of available hardware accelerators. Upon completion, the outputs of all sub-tasks were automatically aggregated and post-processed to reconstruct the full prediction results over the entire volume. For tasks including the segmentation of neurons, synapses, and mitochondria, the block and overlap sizes were set to 8,600 × 8,600 × 31 and 600 × 600 × 1 voxels, with a resolution of 4 × 4 × 33 nm^3 per voxel. For tasks including the segmentation of nuclei and vessels, the block and overlap sizes were set to 1,075 × 1,075 × 31 and 75 × 75 × 1 voxels, with a resolution of 32 × 32 × 33 nm^3 per voxel.

Preprocessing and dense segmentation

To address the Poisson and Gaussian noise inherent in EM images and to overcome the challenges of self-supervised denoising with degraded inputs, we implemented Blind2Unblind for implicit lossless self-supervised denoising[97]. This framework leveraged a mask-guided medium to enhance and denoise EM images. It consisted of a globally-aware mask mapper driven by mask-based sampling and a non-blind lossless training strategy based on re-visible loss. Next, to enhance local 3D continuity and improve inference performance, we adopted a spatial registration strategy inspired by the preprocessing pipeline of the

Flood-Filling Network (FFN)[98]. For each chunk mentioned above, a 4 × 4 affine transformation matrix was estimated to align it with a global reference space. Neural network inference, aggregation, and merging were then performed on the aligned chunks. After dense segmentation, inverse transformations were applied to map the results back to the original coordinate system, followed by cropping to restore the original dimensions. All affine matrices were precomputed and cached prior to processing to reduce computational overhead.

After preprocessing, we employed a boundary detection-based dense segmentation approach to process the whole-brain EM dataset. The image segmentation network adopted a U-shaped architecture with residual blocks, and was trained to predict nearest-neighbor affinity maps along all three spatial dimensions. The training dataset consisted of seven randomly selected volumes, each comprising 30 consecutive sections with a spatial size of 2,000 × 2,000 × 30 voxels at a resolution of 4 × 4 × 33 nm^3. All these volumes were manually annotated by experts. A composite loss function combining weighted cross-entropy and Dice loss was employed to enhance segmentation performance, particularly in the presence of class imbalance. To improve model generalization, we applied a range of data augmentation techniques during training, including basic transformations such as rotation, flipping, and elastic deformation, as well as robustness-oriented strategies such as CutBlur, CutNoise, and Mixup. In addition, we simulated common imaging artifacts including registration shifts, motion blur, and partial slice dropouts, to enhance the model's capability to handle real-world imperfections, thereby improving the stability and accuracy of the segmentation.

Intra-chunk agglomeration

To construct the signature graph, we first performed over-segmentation of the membrane probability map using a 2D watershed algorithm based on distance transform. Specifically, small connected membrane boundary components were removed through thresholding. Given the strong anisotropy of the data (with lateral resolution of 4 nm per voxel and axial resolution of 33 nm per voxel), the Euclidean distance transform was applied to each membrane probability map. The maximum distance value was then used as the seed point to execute the watershed algorithm, producing 2D watershed superpixels. These superpixels were subsequently merged to achieve the 3D reconstruction. The image could be represented using watershed superpixels, where the superpixels served as vertices and the physical connectivity between them formed the edges of a graph model. The superpixel merging problem was thus formulated as a vertex partitioning problem on the graph. In this study, the problem is modeled as the minimum cost multicut problem (MCMP) on the superpixel adjacency graph[99]. For feature extraction, three types of features were manually extracted: boundary features between superpixels, edge features within each superpixel, and inter-layer features derived from the anisotropic dataset. A feature vector of length 625 was designed for each edge between two superpixels. A random forest classifier was then trained to predict the

probability of merging each pair of superpixels. Based on maximum likelihood estimation, the predicted probability is converted into the cost for merging the two superpixels. This resulted in an instance of the multicut problem. Additionally, previously reconstructed and expert-verified whole-brain nucleus and synapse segmentation results were introduced as soft priors[100]. Superpixels belonging to the same nucleus should be merged preferentially, while superpixels on opposite sides of the same synapse should be merged less likely. At the same time, the aggregation range was confined to the effective tissue mask area to prevent the merging of defect regions with other superpixels, thereby avoiding erroneous propagation. Given that the combinatorial optimization problem defined here is NP-hard, and exact methods are not polynomial-time solvable, this study framed the problem as a sequential decision-making task for node aggregation on the graph. The problem was solved optimally using the heuristic greedy additive edge contraction (GAEC) framework[101]. Finally, the results were mapped back to the original over-segmented image obtained from the watershed distance transform.

Inter-chunk stitching

Following the preliminary reconstruction of all individual chunks, we developed an overlap-aware fragment agglomeration algorithm to identify and merge neuronal segments across adjacent chunks, thereby enabling the reconstruction of globally continuous neuronal structures. This algorithm integrated a deep learning-based candidate identification module with a set of rule-based merging constraints. Specifically, we trained a 3D-ResNet-based neural network classifier to evaluate fragment pairs extracted from sliding 3D windows within overlapping regions, producing a probability score indicating whether the pair originated from the same cell. Candidate merges were then further filtered based on multiple criteria, including intersection-over-union (IoU) thresholds, voxel overlap chunk, and the presence of defect masks, to ensure that the final agglomeration decisions maintained both structural continuity and biological plausibility. By combining large-scale parallel processing enabled by the Slurm workload manager mentioned above with this customized post-processing pipeline, we established an efficient workflow for dense reconstruction.

Segmentation of nuclei and vessels

We annotated nuclei and vessels in every fifth section of the downsampled ssEM dataset with a resolution of 32 × 32 × 165 nm^3, generating high-quality training sets with dimensions of 9,000 × 6,000 × 764 voxels. These results were used to train a 2D segmentation network. We employed nnU-Net[102] for training and inference, with a patch size set to 1,024 × 1,024 × 4 and a batch size of 2. To maintain training stability, we chose stochastic gradient descent (SGD) with a momentum of 0.99 as the optimizer and applied a “poly” learning rate policy, starting with a learning rate of 0.01 and a maximum of 1,000 epochs. Upon completion of inference, we restored the results to the original space, resulting in a coarse reconstruction of the entire volume. Next, we implemented a sliding window strategy along the z-axis, systematically

traversing connected instances within each window, to achieve a refined reconstruction of the whole-brain nuclei and vessels. The window length was set to 30, with an overlap of 4. When the number of voxels within the receptive field was less than 1000, the z-axis voxel range was under 2, or the instance did not contact adjacent windows, we classified it as reconstruction noise and removed it. Approximately 35% of nuclei and all vessels underwent further manual proofreading, followed by quantitative analysis and 3D visualization.

Nucleus clustering

We developed a feature extraction pipeline, integrating both traditional handcrafted morphological features and high-level representations learned through self-supervised learning, to analyze whole-brain nuclei with diverse morphologies. Manually-proofread 176,789 nuclei (nuclei with incomplete structures in rostralmost and caudalmost sections were excluded) were processed using the CloudVolume framework to compute 3D surface meshes and then extracted 13 traditional morphological features using the Trimesh library. These 13 features collectively characterized nucleus compactness (Φ, κ_A, κ_V), surface irregularity (ΔA, ΔA_b), shape elongation (ρ_{max}, R_{range}), and spatial dispersion (r_{max}, r_{min}). The following notations were adopted:

M: 3D triangular mesh representing a nucleus surface.

V: Volume of the nucleus mesh (μm³).

A: Surface area of the nucleus mesh (μm²).

C: Geometric centroid of the nucleus mesh.

M_h: Convex hull mesh of M.

V_h, A_h: Volume and surface area of convex hull, respectively.

S_b: Minimal bounding sphere of M.

V_b, A_b: Volume and surface area of bounding sphere, respectively.

v_i: i-th vertex of mesh M.

$\|\cdot\|$: Euclidean norm in $\mathbb{R}^3$.

Φ: Sphericity defined as $\Phi = \pi^{1/3}(6V)^{2/3}/A$, where $\Phi \in [0, 1]$ and $\Phi = 1$ defines a perfect sphere.

κ_A: Surface convexity defined as $\kappa_A = A/A_h$

κ_V: Volume convexity defined as $\kappa_V = V/V_h$

ΔA: Surface concavity defined as $\Delta A = A - A_h$

ΔV: Volume concavity defined as $\Delta V = V_h - V$

ρ_{max}: Elongation ratio defined as $\rho_{max} = \max_i(\|v_i - C\|)/\min_i(\|v_i - C\|)$

R_{range}: Radial range defined as $R_{range} = \max_i(\|v_i - C\|) - \min_i(\|v_i - C\|)$

r_{max}: Normalized max radius defined as $r_{max} = (\max_i(\|v_i - C\|))^3/V$

r_{min}: Normalized min radius defined as $r_{min} = (\min_i(\|v_i - C\|))^3/V$

σ_A: Spherical area ratio defined as $\sigma_A = A/A_b$

σ_V: Spherical volume ratio defined as $\sigma_V = V/V_b$

ΔA_b: Spherical surface excess defined as $\Delta A_b = A_b - A$

ΔV_b: Spherical volume excess defined as $\Delta V_b = V_b - V$

e: Eccentricity computed based on principal component analysis of the mesh vertices as $e = \sqrt{1 - \frac{\lambda_{min}}{\lambda_{max}}}$, where λ_{max} and λ_{min} are the largest and smallest eigenvalues of the mesh vertex covariance matrix, respectively.

To complement these interpretable handcrafted features, a self-supervised deep learning framework was implemented to extract high-level geometric representations of the nucleus shape. Unlike voxel- or mesh-based formats, point clouds provide a compact and resolution-independent representation that preserved fine morphological details. Each nucleus surface mesh M was uniformly sampled using Poisson disk sampling in Trimesh to obtain a point cloud $P \in \mathbb{R}^{n\times 3}$, where n = 3,072 represented the number of sampled vertices. The sampling process ensured uniform spatial distribution across the mesh surface while preserving geometric details. The point clouds were processed using a Siamese self-supervised architecture based on SimSiam[103] to learn transformation-invariant descriptors. During training, each point cloud P was augmented into two distorted views P_1 and P_2 using random rotations, Gaussian noise, and jittering. The augmented views were processed through a three-stage neural network pipeline:

$$f: \mathbb{R}^{n\times 3} \rightarrow \mathbb{R}^{d} \rightarrow g: \mathbb{R}^{d} \rightarrow \mathbb{R}^{d'} \rightarrow h: \mathbb{R}^{d'} \rightarrow \mathbb{R}^{d'}$$

where $f(\cdot)$ (Encoder network, PointNet-based backbone) mapped point clouds to d = 1,024-dimensional embeddings, $g(\cdot)$ (Projector network, 2-layer MLP) mapped to d' = 256-dimensional projections, and $h(\cdot)$ (Predictor network, 2-layer MLP) with same dimensionality. The model was trained to minimize a symmetric negative cosine similarity loss:

$$\mathcal{L} = -\tfrac{1}{2}[D(h(g(f(P1))), \underline{g(f(P2))}) + D(h(g(f(P2))), \underline{g(f(P1))})]$$

where $D(x, y) = x\cdot y/(||x||_2\ ||y||_2)$ denoted the cosine similarity function. The underlined terms were treated as constants during backpropagation and did not contribute gradients. This objective encouraged the network to learn rotation- and noise-invariant representations while preventing representational collapse. Each nucleus was ultimately represented by a d = 1,024-dimensional embedding vector $z = f(P)$ extracted from the trained encoder. To reduce redundancy and enable integration with handcrafted features, we applied Uniform Manifold Approximation and Projection (UMAP)[104] with the following hyperparameters (Target dimensionality: d_{UMAP} = 8; Number of neighbors: k = 15; Minimum distance: d_{min} = 0.1; Distance metric: Euclidean). This yielded an 8-dimensional deep feature representation $z_{UMAP} \in \mathbb{R}^{8}$ for each nucleus. The final feature representation for each nucleus was constructed by concatenating the 8-dimensional deep feature embedding $z_{UMAP} \in \mathbb{R}^{8}$ with the 13-dimensional handcrafted morphological feature vector $f_{morph} \in \mathbb{R}^{13}$: $f_{hybrid} = [f_{morph}; z_{UMAP}] \in \mathbb{R}^{21}$, where $[\cdot;\ \cdot]$ denoted vector concatenation. Prior to concatenation, all features were standardized using z-score normalization: $f' = (f - \mu)/\sigma$, where μ and σ represented the mean

and standard deviation computed across the entire dataset, respectively. This hybrid descriptor f_{hybrid} leveraged both interpretable morphological traits (providing biological insight) and high-capacity deep embeddings (capturing complex geometric patterns), enabling robust and scalable analysis of nucleus morphology.

Similarly, we adopted the same methodology for morphological analysis of somata. Since somata could be characterized with the aid of associated structures such as nuclei and mitochondria, the computation of traditional somatic features incorporated not only the aforementioned morphological descriptors but also integrated nucleus- and mitochondria-based features as auxiliary representations.

Segmentation of PSDs, SVs, and mitochondria

A three-class 3D U-Net network was trained to predict PSDs and SVs at the resolution of 8 × 8 × 33 nm^3 per voxel. We annotated four regions (~12 × 12 × 1 μm^3 per volume), generating training sets encompassing 146M voxels. We optimized the network using the multi-class cross-entropy loss and SGD optimizer. During training, a warm-up learning rate strategy was employed with an initial learning rate of 0.01, a linear warm-up period of 2k steps, and cosine decay over a total of 500k training steps. Data augmentation was performed to improve the network's robustness, including random rotation, random flipping, grayscale transformation, elastic transformation, and blur simulation. To test the network performance, we manually annotated another three regions as test sets (~8 × 8 × 1 μm^3 per volume). The evaluation of these regions yielded an average precision of 85.60 ± 3.21% and an average recall of 88.37 ± 1.59%.

A 3D U-Net network was trained to detect the mitochondria at the resolution of 8 × 8 × 33 nm^3 per voxel. We annotated five regions (~12 × 12 × 1 μm^3 per volume), generating training sets encompassing 467M voxels. To separate adjacent mitochondria, we designed a network to simultaneously predict both a mitochondrial mask (trained with binary cross-entropy loss) and an instance boundary mask (optimized using a combined binary cross-entropy and Dice loss). Training proceeded for 500k iterations with SGD optimizer, applying a learning rate scheduling strategy identical to the synapse detection task. Data augmentation protocols were consistently implemented as in the synapse detection framework. For automated identification of glycinergic neurons, we annotated additional 284 soma-localized mitochondria labeled with APEX2. Neurons were classified as glycinergic if their somata contained ≥ 4 labeled mitochondria.

Proofreading

We conducted extensive manual and semi-automated proofreading of neurons, PSDs, SVs, mitochondria, vessels, and brain regions using a custom software Advanced Connectome Engine (ACE) that integrated the Hadoop- and HBase-based data management, computing modules, and collaborative tools. We used this software to coordinate proofreading tasks, facilitate collaborative proofreading workflows, and log all user operations. Current and

immediately preceding proofreading results were compared to evaluate proofreaders' performance. The proofreading team consisted of 30 – 40 full-time proofreaders from commercial companies and several experts from the laboratories involved. Reconstruction results were represented as graph structures that connected segmentation contours across all serial sections belonging to a single supervoxel. The contours of adjacent layers were compared to identify anomalies and guide proofreaders to target regions requiring correction.

To aid the proofreading workflow, we utilized a series of foundation models for segmentation[105-107], including the Segment Anything Model (SAM), SAM 2 and SAEM². Based on these models, we implemented two additional strategies to enhance ACE's human-computer interaction. First, the SAM ViT-H model checkpoint was exported to an ONNX (Open Neural Network Exchange) model with additional quantization and optimization. ONNX Runtime was used to execute these models on CPU/GPU, which supported cross-platform inference and improved software runtime. Second, the SAM embeddings generated by encoders were precomputed and saved in CloudVolume using kempressed format, which demonstrated higher compression ratios compared to raw and fpzip encodings. For 2D semi-automated segmentation, we utilized manually traced neuronal skeletons with extra positive/negative points as input prompts for the SAM model. However, the pretrained SAM failed to accurately segment densely packed, homogeneous neuronal processes[108]. To address this, we proposed the finetuned SAEM² with auxiliary tasks to acquire complementary multi-head information for neuron segmentation in the ssEM dataset. The auxiliary task involved identifying cell boundaries (plasma membranes) to complement the original SAM that primarily focused on cell masks. For 3D segmentation, we employed the SAM 2 augmented with two additional strategies: (1) We trained the system to predict cross-correlation maps and subsequently computed the shifts between adjacent 2D EM images. (2) We utilized the distance transformation maps from the previous cell masks to sample prompt points for generating the next cell masks.

Micro-mesoscopic morphology comparison

We inferred the neuronal types of APEX2-unlabeled neurons based on morphology comparison between the ssEM dataset and the Zebrafish Mesoscopic Atlas[20]. A preprocessed reference file was generated, containing the x-y-z coordinates of all E and I neurons and their mirrored counterparts from the Zebrafish Mesoscopic Atlas (n_{Glu} = 12,219, n_{GABA} = 5,371, n_{Gly} = 2,193). We first calculated neuronal skeletons (stored as swc files) from manually-corrected EM supervoxels. These skeletons were then transformed into the common physical space of the mesoscopic brain template using bidirectional CLEM approach mentioned above. Using the soma center of each EM query neuron as the origin, we retrieved all single-neuron morphological data within a 25 μm spherical radius based on the preprocessed reference file. For each EM query neuron, we performed pairwise morphology comparisons with the retrieved mesoscopic reference neurons. Cross-scale skeleton matching established

morphological correspondences between the same type of neurons across imaging modalities by quantifying spatial relationships between their reconstructed skeletons. The matching similarity was constructed by calculating the unidirectional distance (D) from EM skeletons (S_E) to LM skeletons (S_L) as follows,

$$D=\frac{1}{|S_E|}\sum_{p\in S_E} D_{min}(p,S_L)$$

where D_{min} represents the shortest distance from S_L to the point p in S_E. The distance for each point in S_E was calculated, and the average was then determined. The S_L that minimized D was chosen as the most similar skeleton corresponding to S_E. This distance-based scoring system ranked similarity (lower scores indicated closer matches), with the top-ranked matches (swc filenames and scores) exported. These results were manually verified using a custom software Brain Atlas Viewer (BrAVe)[21].

3D visualization

In accordance with open-science principles, we employed the Neuroglancer precomputed format and CloudVolume interface for data management and 3D visualization through both Neuroglancer and webKnossos[109]. For data encoding, we used JPEG compression for ssEM images and compressed_segmentation format for region silhouettes and segmentation masks. We further implemented the Igneous[110] for multiprocessed block-wise downsampling, skeletonization and meshing with the following agglomeration. For skeletonization, we used the Kimimaro implementation of the automated TEASAR algorithm[111]. We then merged the skeleton splits that might appear based on nearest Euclidean neighbors, calculated the path length of the skeleton, and determined the radius of each vertex in the skeleton. For meshing, we used the automated block-wise Zmesh to generate multi-resolution meshes. These skeletons and meshes were stored in sharded formats.

We employed mesh representations to visualize brain regions and reconstructions in Neuroglancer, while utilizing annotation points to demonstrate synaptic locations. The Neuroglancer *matrix* function served as an affine transformation tool for manipulating (translate/flip/rotate/zoom) the original image layers. We used the parallel projection during Neuroglancer rendering to generate 3D scale bars. Furthermore, we optimized two existing workflows for video creation: (1) Neuroglancer workflow using Python scripts from the *video_tool* package, and (2) the open-source computer graphics software Blender, with Python scripts and JSON descriptions from neuVid. Since we acquired high-resolution images only for the retina, optic nerve, brain and anterior SC, we processed a pre-acquired low-resolution dataset (400 × 400 × ~1,650 nm^3 per voxel) of the complete zebrafish head to provide comprehensive 3D rendering context used in Fig.1b and Supplementary Video 1. We first verified the section number corresponding to the whole-brain high-resolution dataset, and then generated uniformly spaced, downsampled images (992 × 992 × 660 nm^3 per voxel) along the rostral-caudal axis using linear interpolation. These images were subsequently

registered to the high-resolution dataset, ensuring alignment with multiple segmentation and reconstruction results within the same physical space. Finally, grayscale histogram equalization was performed. The ssEM dataset are accessible through the following dedicated links:

https://ng.zebrafish.digital-brain.cn/Fish-X/Brain_EM_images
https://ng.zebrafish.digital-brain.cn/Fish-X/Retina_EM_images
https://ng.zebrafish.digital-brain.cn/Fish-X/Brain_regions
https://ng.zebrafish.digital-brain.cn/Fish-X/Auto_supervoxels
https://ng.zebrafish.digital-brain.cn/Fish-X/Manual_supervoxels
https://ng.zebrafish.digital-brain.cn/Fish-X/Nuclei
https://ng.zebrafish.digital-brain.cn/Fish-X/Vessel

Statistical analysis

No randomization and blinding were used during data collection and analysis. The statistical analysis was performed using GraphPad Prism. Error bars represent mean ± SEM. Kolmogorov-Smirnov test was used for testing normality. Two-tailed Mann Whitney U test was used in Figs. 2d,j, 3k, 4e, and Extended Data Figs. 5d, 9c. Two-tailed two-sample Kolmogorov-Smirnov test was used in Fig. 4j,k,w. Linear regression analysis was used in Figs. 3d,l,m, 4f,g, and Extended Data Fig. 6d-f. Exponential fitting was performed in Fig. 4n. Chi-square goodness-of-fit test was performed in Fig. 4q. Statistical significance is defined as $P < 0.05$. The specific statistical tests, P-value ranges, and sample sizes are provided in the corresponding figures and/or figure legends.

Reporting summary

Further information on research design is available in the Nature Port-folio Reporting Summary linked to this article.

Data availability

Plasmids, zebrafish lines, and the ssEM dataset generated in this study will be available upon request.

Code availability

All source codes and algorithms are available at https://github.com/MiRA-Han-Lab/Fish-X.

References (Methods)

79. McLean, D. L., Fan, J., Higashijima, S., Hale, M. E. & Fetcho, J. R. A topographic map of recruitment in spinal cord. *Nature* **446**, 71-75 (2007).
80. Prober, D. A., Rihel, J., Onah, A. A., Sung, R. J. & Schier, A. F. Hypocretin/orexin overexpression induces an insomnia-like phenotype in zebrafish. *J. Neurosci.* **26**, 13400-13410 (2006).
81. Asakawa, K. et al. Genetic dissection of neural circuits by Tol2 transposon-mediated Gal4 gene and enhancer trapping in zebrafish. *Proc. Natl. Acad. Sci. U. S. A.* **105**,

1255-1260 (2008).
82. Quirin, S. et al. Calcium imaging of neural circuits with extended depth-of-field light-sheet microscopy. *Opt. Lett.* **41**, 855-858 (2016).
83. Muto, A. et al. Activation of the hypothalamic feeding centre upon visual prey detection. *Nat. Commun.* **8**, 15029 (2017).
84. Li, J. et al. Intron targeting-mediated and endogenous gene integrity-maintaining knockin in zebrafish using the CRISPR/Cas9 system. *Cell Res.* **25**, 634-637 (2015).
85. Shang, C.-F. et al. Real-time analysis of large-scale neuronal imaging enables closed-loop investigation of neural dynamics. *Nat. Neurosci.* **27**, 1014-1018 (2024).
86. Kawakami, K. Tol2: a versatile gene transfer vector in vertebrates. *Genome Biol.* **8**, S7 (2007).
87. Ariotti, N. et al. Modular Detection of GFP-labeled proteins for rapid screening by electron microscopy in cells and organisms. *Dev. Cell.* **35**, 513-525 (2015).
88. Martell, J. D., Deerinck, T. J., Lam, S. S., Ellisman, M. H. & Ting, A. Y. Electron microscopy using the genetically encoded APEX2 tag in cultured mammalian cells. *Nat. Protoc.* **12**, 1792-1816 (2017).
89. Willingham, M. C. & Rutherford, A. V. The use of osmium-thiocarbohydrazide-osmium (OTO) and ferrocyanide-reduced osmium methods to enhance membrane contrast and preservation in cultured cells. *J. Histochem. Cytochem.* **32**, 455-460 (1984).
90. Hua, Y.-F., Laserstein, P. & Helmstaedter, M. Large-volume en-bloc staining for electron microscopy-based connectomics. *Nat. Commun.* **6**, 7923 (2015).
91. Xin, T., Shen, L.-J., Li, L.-L., Chen, X. & Han, H. Expected affine: A registration method for damaged section in serial sections electron microscopy. *Front. Neuroinform.* **16**, 944050 (2022).
92. Lowe, D. G. Distinctive image features from scale-invariant keypoints. *Int. J. Comput. Vis.* **60**, 91-110 (2004).
93. Fischler, M. A. & Bolles, R. C. Random sample consensus: a paradigm for model fitting with applications to image analysis and automated cartography. *Commun. ACM.* **24**, 381-395 (1981).
94. Saalfeld, S., Fetter, R., Cardona, A. & Tomancak, P. Elastic volume reconstruction from series of ultra-thin microscopy sections. *Nat. Methods* **9**, 717-720 (2012).
95. Duchon, J. Splines minimizing rotation-invariant semi-norms in Sobolev spaces. In *Constructive Theory of Functions of Several Variables* (eds Schempp, W. & Zeller, K.) **571**, 85-100 (Springer, Berlin, Heidelberg, 1977).
96. Besl, P. J. & McKay, N. D. A method for registration of 3-D shapes. *IEEE Trans on Pattern Analysis and Machine Intelligence* **14**, 239-256 (1992).
97. Wang, Z.-J., Liu, J.-Z., Li, G.-Q. & Han, H. Blind2unblind: Self-supervised image denoising with visible blind spots. In *Proc. IEEE/CVF Conference on Computer Vision and Pattern Recognition (CVPR)* 2027-2036 (IEEE, 2022).
98. Januszewski, M. et al. High-precision automated reconstruction of neurons with flood-filling networks. *Nat. Methods* **15**, 605-610 (2018).
99. Beier, T. et al. Multicut brings automated neurite segmentation closer to human performance. *Nat. Methods* **14**, 101-102 (2017).
100. Hong, B. et al. Graph partitioning algorithms with biological connectivity decisions for

neuron reconstruction in electron microscope volumes. *Expert Syst. With Applic.* **222**, 119776 (2023).

101. Keuper, M. et al. Efficient decomposition of image and mesh graphs by lifted multicuts. In *Proc. IEEE/CVF International Conference on Computer Vision (ICCV)* 1751-1759 (IEEE, 2015).
102. Isensee, F., Jaeger, P. F., Kohl, S. A., Petersen, J. & Maier-Hein, K. H. nnU-Net: a self-configuring method for deep learning-based biomedical image segmentation. *Nat. Methods* **18**, 203-211 (2021).
103. Chen, X.-L. & He, K.-M. Exploring simple siamese representation learning. In *Proc. IEEE/CVF Conference on Computer Vision and Pattern Recognition (CVPR)* 15750-15758 (IEEE, 2021).
104. McInnes, L., Healy, J. & Melville, J. UMAP: uniform manifold approximation and projection for dimension reduction. Preprint at https://arxiv.org/abs/1802.03426 (2018).
105. Kirillov, A. et al. Segment anything. In *Proc. IEEE/CVF International Conference on Computer Vision (ICCV)* 4015-4026 (IEEE, 2023).
106. Ravi, N. et al. Sam 2: Segment anything in images and videos. In *13th International Conference on Learning Representations (ICLR)* (2025).
107. Zhai, H., Guo, J.-Y., Zhang, Y.-C, Liu, J. & Han, H. SAvEM 3: Pretrained and Distilled Models for General-purpose 3D Neuron Reconstruction. In *2024 IEEE International Conference on Bioinformatics and Biomedicine (BIBM)* 3972-3977 (IEEE, 2024).
108. Januszewski, M. & Jain, V. Next-generation AI for connectomics. *Nat. Methods* **21**, 1398-1399 (2024).
109. Boergens, K. M. et al. webKnossos: efficient online 3D data annotation for connectomics. *Nat. Methods* **14**, 691-694 (2017).
110. Silversmith, W. et al. Igneous: Distributed dense 3D segmentation meshing, neuron skeletonization, and hierarchical downsampling. *Front. Neural Circuits* **16**, 977700 (2022).
111. Sato, M., Bitter, I., Bender, M. A., Kaufman, A. E. & Nakajima, M. TEASAR: tree-structure extraction algorithm for accurate and robust skeletons. In *Proc. 8th Pacific Conference on Computer Graphics and Applications* 281-449 (IEEE, 2000).

Acknowledgements

We are grateful to Drs. Jie He, Misha Ahrens, Koichi Kawakami, and Joe Fetcho for sharing fish lines, and Yun-Feng Hua, Jun Zhang, Xiao-Hong Xu, Ke Zhang, Yu Mu, Dan-Qian Liu, Kai Yang, and Sheng-Xiong Wang for insightful advice. We would like to thank Xu-Long Wen, and other staffs from Grand View (Beijing) Technology Co., Ltd, and Zhi Zeng, Le Wang, and other staffs from Chengdu Huizhong Tianzhi Tech. Co., Ltd. (www.hztzai.com) for proofreading. We would like to thank Yu Kong, Li-Jun Pan, Xu Wang, Xue Xu from Electron Microscopy Core Facility (CEBSIT) for assistance in sample preparation, Ming-Quan Chen and Hong-Li Wan from Facility of Mapping Brain-Wide Mesoscale Connectome (FMBWMC, CEBSIT) for assistance in utilizing the Zebrafish Mesoscopic Atlas, Ting-Ting Zhao and Yong-Wei Zhong from FMBWMC for quality assessment of automated segmentation results,

Jia-Wen Huang, Liu-Qin Qian, Chen-Xi Jin, and other staffs from Big Data of Brain Atlas Facility (CEBSIT) for establishing a web-sharing platform, Qian Hu from Optical Imaging Core Facility (CEBSIT) for optical imaging and image processing support, Jia Li for suggestion on fish line generation and cell type identification, Chun-Feng Shang, Rong-Wei Zhang, Yu-Fan Wang, Sha Li, Le Sun, Qiu-Sui Deng, Li-Jun Chen for discussions, Ji-Wen Bu and Ye Hua for lab management, Yan-Hua Zhu from Shanghai Jiao Tong University for supporting X-ray tomography. We thank our institute (CEBSIT) for providing access to GeminiSEM 300 (Zeiss, Germany), Talos L120C TEM (Thermo Scientific, USA), JEM-1230 TEM (JEOL, Japan), FV3000 confocal laser scanning microscope (Olympus, Japan), and high-performance computing capabilities at the Center for Data and Computing in Brain Science. We thank the Transdisciplinary Platform of Functional Connectome and Brain-Inspired Intelligence in Huairou Science City in Beijing and the Microscopic Technology & Analysis Center at the Institute of Automation, Chinese Academy of Sciences for providing technical support and device resources. This work was supported by National Science and Technology Innovation 2030 Major Program of the Ministry of Science and Technology (2021ZD0204500, 2021ZD0204502 and 2021ZD0204503), Creative Research Groups (32321003) and general grant (32171461) of the National Natural Science Foundation of China, Shanghai Municipal Science and Technology Major Project (18JC1410100 and 2018SHZDZX05), and Key Research Program of Frontier Sciences (QYZDYSSW-SMC028) and Strategic Priority Research Program (XDB32010200) of Chinese Academy of Sciences.

Author contributions

J.L.D., H.H., and F.N.L. conceived and supervised the project. F.N.L. and J.L.D. wrote the manuscript with input from H.H., J.Z.L., C.S., J.B.Y., J.L., Y.N.L., Y.C.Z., H.Y.Y., H.Z., L.L.L., L.N.Z., and X.H.D. F.N.L. generated APEX2 fish lines, prepared samples, analyzed the LC-NE system's input organization, and coordinated proofreading and discussions. J.Z.L. performed whole-brain automated reconstruction including nuclei and vessels. C.S. generated and managed APEX2 fish lines, prepared samples, and summarized all manually verified reconstructions. J.B.Y. was responsible for the data management and proofreading system maintenance. Y.N.L. performed image registration including CLEM. J.L. performed automated segmentation of PSDs, SVs, and mitochondria. L.N.Z. performed image acquisition. L.L.L. collected sections. L.J.S. supported proofreading system maintenance. X.C. supported image registration. H.Z. conducted skeletonization and 3D visualization. Y.C.Z. executed nucleus clustering. R.K.T. and H.Y.H. generated APEX2 plasmids. F.X.Z., T.X., B.H.C., H.R.C., and S.C. participated in image registration. T.X. performed image repair. B.H.C. handled image denoising and interpolation of the low-resolution EM dataset. H.T.M. performed ion milling. H.Y.Y. and J.L.Z. carried out micro-mesoscopic morphology comparison. J.Y.G. participated in vessel segmentation. Z.H.F. and Y.S.W. contributed to proofreading. X.H.D. assisted in section collection. L.M.L. assisted in image acquisition.

X.H.Z. supported remote proofreading management. C.Y.Q. performed immunostaining. S.R.J. annotated retinal regions. C.M.Z., P.S.X., and Y.X.Y. contributed to the analysis of the LC-NE system. Y.Q. and Y.C.G. participated in discussions. X.F.D. supported the utilization of the Zebrafish Mesoscopic Atlas and BrAVe. Q.W.X. contributed to reconstruction.

Competing interests

The authors declare no conflict of interest.

1387 ## Figure Legends

1388 **Fig. 1 | Multiplexed NM-type-labeled whole-brain ssEM of larval Zebrafish.**
1389 **a,** Schematic of multiplexed EM neuronal-type annotation in APEX2-labeled zebrafish larvae.
1390 Subcellular-localized APEX2 conjugated TagRFP (bottom left, red) catalyzes the conversion
1391 of DAB into osmiophilic substances, creating localized non-transmembrane electron densities
1392 (bottom right, black) within specific neuronal types and generating distinct EM-visible
1393 patterns.
1394 **b,** Rendering of the intact head (left, 992 × 992 × 660 nm^3 per voxel) and representative EM
1395 images of the right retina (bottom right, 32 × 32 nm^2 per pixel), right optic nerve (upper center,
1396 8 × 8 nm^2 per pixel resolution), and anterior spinal cord (upper right, 32 × 32 nm^2 per pixel)
1397 in a 6-dpf larva.
1398 **c,** Rendering of manually corrected brain-wide neural tracts (yellow) and vessels (light red).
1399 Most vessels remained well-preserved, though some collapse was observed in the
1400 telencephalon. Neural tracts, identified as a bundle of parallel-oriented fibers, were manually
1401 traced. Vessels were automatically reconstructed, followed by manual proofreading.
1402 **d,** Grayscale-coded projected nucleus density along three axes. In the brain, 176,810 nuclei
1403 that were automatically segmented and subsequently manually proofread were used for
1404 analysis.
1405 **e,** Rendering of randomly color-coded nuclei distributed across four representative horizontal
1406 planes along dorsal-ventral axis (interval, 50 μm). The dorsal-ventral distance is relative to
1407 the epidermal surface.
1408 **f,** Rendering of the reconstruction of 523 manually-proofread brain-wide neurons. These
1409 include 13 NE neurons in the LC and MO (orange; $n_{LC\text{-}NE}$ = 10, $n_{MO\text{-}NE}$ = 3), 10 DA neurons in
1410 the OB, PT and Hc (light green; $n_{OB\text{-}DA}$ = 3, $n_{PT\text{-}DA}$ = 4, $n_{Hc\text{-}DA}$ = 3), 7 5HT neurons in the Pr
1411 and RN (dark blue; $n_{Pr\text{-}5HT}$ = 3, $n_{RN\text{-}5HT}$ = 4), 2 Hcrt neurons in the hypothalamus (magenta),
1412 24 Gly neurons in the midbrain and hindbrain (sky blue), 178 Glu neurons (purple), 38
1413 GABA neurons (green), 247 unidentified neurons (light gray), 3 RGCs (red), and one M-cell
1414 (dark gray).
1415 C, caudal; L, left; V, ventral. LC, locus coeruleus; MO, medulla oblongata; OB, olfactory
1416 bulb; PT, posterior tuberculum; Hc, caudal hypothalamus; Pr, pretectum; RN, raphe nucleus.
1417 NE, noradrenergic; DA, dopaminergic; 5HT, serotonergic; Hcrt, hypocretinergic; Gly,
1418 glycinergic; Glu, glutamatergic; GABA, GABAergic; RGC, retinal ganglion cell; M-cell,
1419 Mauthner cell. See also Extended Data Figs. 1,2, and Supplementary Video 1.
1420

1421 **Fig. 2 | APEX2 labeling- and mesoscopic atlas-based neuronal type identification.**
1422 **a,** Schematic of three strategies for neuronal type identification based on APEX2 labeling
1423 (top), intrinsic properties (middle), and mesoscopic atlas comparison (bottom).
1424 **b,** Representative EM images of all types of APEX2-labeled neurons (4 × 4 nm^2 per pixel).

1425 Individual APEX2-labeled neurons display various degrees of staining intensity and are
1426 contoured by color-coded dashed lines. Two APEX2-labeled mitochondria in a Gly neuron are
1427 indicated by white arrows, one of which is located near the infoldings of the nucleus. The
1428 rostral-caudal locations of related sections are shown (bottom right).
1429 **c,** Rendering of a single LC-NE neuron's soma, containing endoplasmic reticulum (ER,
1430 orange), Golgi apparatus (GA, pink), mitochondria (Mito, light blue), nucleus (light green),
1431 nucleolus (red), and a primary cilia. The Mito (top right) and ER (bottom right) are depicted
1432 separately.
1433 **d,** Distinct relationship between the nucleus-to-soma volume ratio and somatic mitochondrial
1434 density for APEX2-labeled LC-NE neurons (orange, n = 5) and adjacent unlabeled cells (gray,
1435 n = 69). The blue arrow points to an unlabeled cell, which displays similar properties to those
1436 of LC-NE neurons and is speculated to be an unlabeled LC-NE neuron.
1437 **e,** UMAP visualization of clustering of all cells in **d** using combined deep-learned and
1438 traditional features of their nuclei and somata. The blue arrow in the inset points to the same
1439 unlabeled cell indicated in **d**.
1440 **f,** Rendering of the five APEX2-labeled (orange) and one unlabeled (blue) LC-NE neurons
1441 shown in **d,e**. Morphological reconstruction reveals similar axonal projection patterns
1442 between the LC-NE neuron #3 and unlabeled LC-NE neuron.
1443 **g-i,** Representative examples showing partially EM-reconstructed query neurons (black) with
1444 their fully LM-reconstructed top-ranked E (Glu, magenta) or I (GABA, green; Gly, blue)
1445 counterparts, revealed by morphology comparison. Some EM queries are matched to LM
1446 neurons with similar morphology (**g,h**), whereas others exhibit substantial morphological
1447 differences from their top-ranked LM references (**i**). All EM queries are presynaptic neurons
1448 to the five LC-NE neurons in the right hemisphere and distributed in brain-wide regions (in
1449 parentheses).
1450 **j,** Comparison of the normalized top penalty scores for all 467 EM queries, with lower
1451 penalty scores indicating higher degrees of matching. The penalty score was normalized by
1452 skeleton node number of EM queries. All results were manually verified after morphological
1453 matching and categorized into E/I-specific match, E/I-ambiguous match, and Un-match. In
1454 some brain regions, E and I neurons exhibit similar morphology, causing good matches
1455 between EM queries and both E/I neurons. Mann Whitney test was performed, and the error
1456 bars represent mean ± SEM.
1457 **k,l,** EM query neuron #41 (black), which exhibits morphology similar to adjacent
1458 LM-reconstructed Glu, GABA, and Gly neurons (**k**; Glu, magenta; GABA, green; Gly, blue)
1459 but is identified as a Gly neuron by mitochondrial-APEX2 labeling (**l,** white arrows).
1460 L, left; Ro, rostral; V, ventral. ER, endoplasm reticulum. See also Extended Data Figs. 3,4,5,
1461 Supplementary Video 2, and Supplementary Tables 1,2,3.
1462
1463 **Fig. 3 | Regional- and NM type-distinct synaptic organization.**

1464 **a,** Co-occurrence of PSDs (25.25 million), SVs (15.77 million), and mitochondria (13.73
1465 million, Mito) in the brain. Automatic 3D reconstructed supervoxels were utilized to assess
1466 whether identified PSDs, SVs, and mitochondria were situated within the same synaptic
1467 compartments.
1468 **b,** Representative EM image (4 × 4 nm^2 per pixel) of a synapse with PSD (blue arrow), SV
1469 (orange dashed line), and a mitochondrion (green dashed line).
1470 **c,** Synapse density distribution across 52 major brain regions. Regions are arranged primarily
1471 along a rostral-to-caudal axis and from sensory-related to motor-related areas. 23.62 million
1472 synapses exhibiting co-occurrence of PSDs and SVs were used for analysis. Multiple PSDs
1473 usually corresponded to a single SV cloud, resulting in a situation where the number of
1474 presumable synapses (23.62 millions) exceeds the number of SVs (15.77 millions).
1475 **d,** Linear regression analysis of synapse density versus nucleus density across 52 brain
1476 regions. The solid line represents the fitted regression line ($Y = -173.3 \times X + 1{,}549$, $R^2 =$
1477 0.7070, $P < 0.0001$), and dashed lines indicate the 95% confidence interval of the fit. Each
1478 circle represents an individual brain region.
1479 **e,** Lognormal frequency distribution of the volume of synaptic components, including PSDs
1480 (blue), SVs (orange), and Mito (green), across the brain. The volume was calculated using the
1481 results of automatic segmentation in Supplementary Tables 4,5,6, and the data from all 52
1482 regions were pooled together.
1483 **f-h,** Lognormal distribution of the probability density for the volumes of PSDs (top), SVs
1484 (middle), and Mito (bottom) in the forebrain (**f**), midbrain (**g**), and hindbrain (**h**). Regions Ep
1485 (brown, **f**) and LCa (cyan, **h**) are indicated by arrows.
1486 **i,j,** Rendering of EM reconstructions for APEX2-labeled NM neurons within the right
1487 hemisphere, including LC-NE and MO-NE neurons (orange), OB-DA, PT-DA and Hc-DA
1488 neurons (light green), Pr-5HT and RN-5HT neurons (blue), and Hcrt neurons (magenta). Gly
1489 neurons with APEX2 labeling, which were identified as LC-NE presynaptic neurons during
1490 reconstruction, are also shown (cyan). Presynaptic input sites are marked as small gray cycles.
1491 The dendritic arbors were fully reconstructed for LC-NE, PT-DA, and RN-5HT neurons, and
1492 partially reconstructed for the other neurons. Neuron numbers are shown in parentheses.
1493 **k,** Dendritic input densities across different neuronal types. Dendritic input density (per μm):
1494 LC-NE, 0.3493 ± 0.0194; MO-NE, 0.1511 ± 0.0185; OB-DA, 0.0255 ± 0.0094; PT-DA,
1495 0.3420 ± 0.0212; Hc-DA, 0.0415 ± 0.0249; Pr-5HT, 0.0759 ± 0.0249; RN-5HT, 0.3749 ±
1496 0.0413; Hcrt, 0.0747 ± 0.0204; Gly, 0.1228 ± 0.0190. $^*P < 0.05$ (Mann Whitney test). Error
1497 bars represent mean ± SEM.
1498 **l,m,** Linear regression analysis of the total projection length versus the dendritic input density
1499 (**l**, $Y = 15{,}580 \times X + 898.7$, $R^2 = 0.3446$, $P = 0.0965$) and dendritic input number (**m**, $Y =$
1500 $19.82 \times X + 884.4$, $R^2 = 0.6275$, $P < 0.05$). The total projection length was calculated as the
1501 average of three individual neurons from mesoscopic datasets for each neuronal type. The
1502 dendritic input density and number were calculated from the same neurons in **i-k**.

1503 C, caudal; L, left; Ro, rostral; V, ventral. OB, olfactory bulb; P, pallium; S, subpallium; Po,
1504 preoptic region; OTAOS, optic tract and accessory optic system; Pr, pretectum; Ep, epiphysis;
1505 Ha, habenula; DT, dorsal thalamus; VT, ventral thalamus; PT, posterior tuberculum; M2,
1506 migrated posterior tubercular region; Hr, rostral hypothalamus; Hi, intermediate
1507 hypothalamus; DHi, diffuse nucleus of the intermediate hypothalamus; Hc, caudal
1508 hypothalamus; Pit, pituitary; NL, neuropil layers (optic tectum); PL, periventricular cell layer
1509 (optic tectum); T, tegmentum; nMLF, nucleus of medial longitudinal fascicle; nIII,
1510 oculomotor nerve nucleus; TL, torus longitudinalis; TS, torus semicircularis; R1, rhombomere
1511 1; nIV, trochlear nerve motor nucleus; IPN, interpeduncular nucleus; SR, superior raphe; CCe,
1512 corpus cerebelli; Va, valvula cerebelli; EG, eminentia granularis; LCa, lobus caudalis cerebelli;
1513 MON, medial octavolateralis nucleus; R2, rhombomere 2; nVd, dorsal motor nucleus of
1514 trigeminal nerve; R3, rhombomere 3; nVv, ventral motor nucleus of trigeminal nerve; IR,
1515 inferior raphe; R4, rhombomere 4; R5, rhombomere 5; MVN, medial vestibular nucleus; TVN,
1516 tangential vestibular nucleus; nVIIr, rostral facial nerve motor nucleus and octavolateralis
1517 efferent neurons; nVIr, rostral motor nucleus of abducens nerve; R6, rhombomere 6; nVIIc,
1518 caudal facial nerve motor nucleus and octavolateralis efferent neurons; nVIc, caudal motor
1519 nucleus of abducens nerve; R7, rhombomere 7; R8, rhombomere 8; nIX/X,
1520 glossopharyngeal/vagal nerve motor nucleus; VLo, vagal lobe; IO, inferior olive. See also
1521 Extended Data Figs. 6,7,8, Supplementary Videos 3,4,5, and Supplementary Tables 4,5,6.
1522
1523 **Fig. 4 | Spatial organization and shared mode of LC-NE neurons' synaptic input**
1524 **architecture.**
1525 **a,** Rendering of synaptic input sites on the dendrites area of the LC-NE neuron #3. Based on
1526 the soma locations of corresponding presynaptic neurons (PNs), input sites are empirically
1527 classified as sensory-related (blue dots) or motor-related (magenta dots). The same color
1528 scheme is applied to all related data below. Synapses that were traced but not yet reached their
1529 soma are marked as gray dots. Dendritic and axonal processes are color-coded as orange and
1530 gray, respectively. The number in parentheses represent the number of synapses.
1531 **b,** 2D spatial distribution of synaptic inputs on the dendrites of LC-NE neuron #3. In
1532 zebrafish, LC-NE neurons are pseudounipolar neurons, with both axonal and dendritic
1533 processes emerging from a primary branch. The distance between each dot and the soma
1534 represents the path length from each input site to the soma.
1535 **c,** Rendering of all 374 EM-reconstructed PNs, which form 418 synapses on the LC-NE
1536 neuron #3. Sensory-related (blue): 160 neurons, 182 synapses; Motor-related (magenta), 214
1537 neurons, 236 synapses. All synapses at the LC-NE neuron #3 were traced and only those
1538 successfully traced back to their somata were used for analysis.
1539 **d,** Distribution of 374 PNs, located at 32 of all 52 brain regions. Neuron numbers are shown
1540 at the right of each bar. R1 and R2 rank as the two predominant input sources, accounting for
1541 20.86% (78/374) and 10.16% (38/374) of total PNs, respectively.

e, Differential probability distributions of sensory- (blue) and motor-related (magenta) synaptic inputs along dendritic path length, from the soma to distal region. The average distance to the soma are indicated by dashed lines. ****$P < 0.0001$ (Mann Whitney test).

f,g, Linear regression analysis of dendritic path length and the corresponding synaptic strength quantified by PSD volume (**f**) and SV volume (**g**). Sensory-related (blue): PSD volume *vs* path length (**f**, left), $Y = -1.181e4 \times X + 4.927e6$, $R^2 = 0.0627$, $P < 0.001$; SV volume *vs* path length (**g**, left), $Y = -3.283e4 \times X + 9.356e6$, $R^2 = 0.0711$, $P < 0.001$. Motor-related (magenta): PSD volume *vs* path length (**f**, middle), $Y = -2.174e4 \times X + 5.7e6$, $R^2 = 0.1369$, $P < 0.0001$; SV volume *vs* path length (**g**, middle), $Y = -3.611e4 \times X + 8.414e6$, $R^2 = 0.0790$, $P < 0.0001$. Right: probability distributions of PSD volume (**f**) and SV volume (**g**) for both sensory- (blue) and motor-related (magenta) inputs, with dashed lines indicating the average distance to the soma (Mann Whitney test).

h, Analysis of E/I composition ratios in both sensory- (n = 82) and motor-related (n = 106) PNs. Both Glu neurons (purple, n = 135) and GABA neurons (green, n = 33) neurons were inferred through morphological comparison, and Gly neurons (blue) were verified via mitochondrial APEX2 labeling (n = 17) or inferred through morphological comparison (n = 3). PNs with type unknown (UN, n = 186) are displayed as gray.

i, Rendering of all 374 color-coded PNs of the LC-NE neuron #3. Inset: highlighted dendritic input sites.

j,k, Differential distribution of E (left) and I (right) input sites on the dendritic area of the LC-NE neuron #3, for sensory-related (**j**) and motor-related (**k**) inputs. White circles represent the soma. The number in parentheses indicate the number of synapses analyzed. Sensory-related GABA/Gly inputs (**j**, right) and motor-related Glu inputs (**k**, left) are more clustered in distal and proximal areas, respectively. Left-right axis: $P_{\text{sensory-E } vs \text{ sensory-I}} < 0.05$, $P_{\text{motor-E } vs \text{ motor-I}} = 0.1072$, $P_{\text{sensory-E } vs \text{ motor-E}} < 0.001$, $P_{\text{sensory-I } vs \text{ motor-I}} < 0.05$, $P_{\text{sensory-E } vs \text{ motor-I}} = 0.6938$, $P_{\text{sensory-I } vs \text{ motor-E}} < 0.0001$. Dorsal-ventral axis, $P_{\text{sensory-E } vs \text{ sensory-I}} = 0.2084$, $P_{\text{motor-E } vs \text{ motor-I}} = 0.1809$, $P_{\text{sensory-E } vs \text{ motor-E}} = 0.0530$, $P_{\text{sensory-I } vs \text{ motor-I}} = 0.2053$, $P_{\text{sensory-E } vs \text{ motor-I}} = 0.6938$, $P_{\text{sensory-I } vs \text{ motor-E}} < 0.05$. Two-sample Kolmogorov-Smirnov test was performed.

l, Rendering of all 69 EM-reconstructed intra-common presynaptic neurons (intra-CPNs), which form 88 synapses on the LC-NE neuron #3. Sensory-related (blue): 30 neurons, 39 synapses; Motor-related (magenta), 39 neurons, 49 synapses.

m, Regional distribution of 69 intra-CPNs. Neuron numbers are shown at the right of each bar.

n, Cell ratio of intra-CPNs with various innervation numbers. PN numbers are shown on bars. Exponential fitting: $Y = 0.0255 + 28.09 \times e^{-1.816 \times X}$, $R^2 = 0.9973$.

o, Analysis of E/I composition ratios for intra-CPNs with various innervation numbers.

p,q, Cell ratio of intra-CPNs with different innervation combinations (**p**) and intra-CPNs innervating different LC-NE neurons (**q**). Neuron numbers are shown above each bar. All intra-CPNs analyzed innervated the LC-NE neuron #3, and #1, #2, #4, and #5 denote the

other four reconstructed LC-NE neurons. The red symbols represent theoretical cell ratios obtained from 100 iterations of random combinations, using identical cell numbers and matched innervation number distributions. Chi-square goodness-of-fit test was performed (**q**, $\chi^2(3) = 7.8727$, $P < 0.05$). Error bars represent mean ± SEM.

r, Rendering of all 26 EM-reconstructed inter-NM system common presynaptic neurons (inter-CPNs), which form 32 synapses on the LC-NE neuron #3. Sensory-related (blue), 12 neurons, 17 synapses; Motor-related (magenta), 14 neurons, 15 synapses.

s, Regional distribution of 26 inter-CPNs. Neuron numbers are shown at the right of each bar.

t, Heatmap depicting spontaneous calcium activities in LC-NE, PT-DA, and RN-5HT neurons, with Z-scored relative fluorescence changes. Black arrows indicate synchronous spontaneous activities between LC-NE and PT-DA neurons. *Ki(th:GAL4-VP16);Ki(tph2:GAL4FF,cmlc2:EGFP);Tg(UAS:GCaMP6s)* larvae at 6 dpf were used for *in vivo* confocal calcium imaging.

u, Number of inter-CPNs with different NM-type combinations of co-innervation.

v, Analysis of E/I composition ratios for inter-CPNs with different NM-type combinations.

w, Differential distribution of non-CPN (left), intra-CPN (middle), and inter-CPN (right) inputs on the dendrites of the LC-NE neuron #3. White circles represent the soma. The number in parentheses indicate the number of synapses analyzed. Both intra-CPN and inter-CPN inputs favor proximal distributions, whereas non-CPN inputs display a more dispersive distribution. Left-right axis: $P_{\text{non-CPN } vs \text{ intra-CPN}} < 0.0001$, $P_{\text{non-CPN } vs \text{ inter-CPN}} = 0.5716$, $P_{\text{intra-CPN } vs \text{ inter-CPN}} < 0.05$. Dorsal-ventral axis: $P_{\text{non-CPN } vs \text{ intra-CPN}} < 0.001$, $P_{\text{non-CPN } vs \text{ inter-CPN}} < 0.01$, $P_{\text{intra-CPN } vs \text{ inter-CPN}} = 0.3284$. Two-sample Kolmogorov-Smirnov test was performed.

x, Model of dendritic input architecture of LC-NE neurons. Brain-wide inputs are spatially organized in a modality- and strength-dependent manner. E/I inputs prefer proximal and distal areas, respectively. And shared inputs within NE/DA/5HT systems innervate more proximal areas.

C, caudal; D, dorsal; L, left; Ri, right; Ro, rostral; V, ventral. See also Extended Data Figs. 9,10,11, and Supplementary Videos 6,7.

1610 ## Extended Data Figure Legends

1611 **Extended Data Fig. 1 | Multiplexed APEX2-labeled fish line and validation.**
1612 **a,** Summary of distinct APEX2-labeling patterns (red) in different neuronal types in the
1613 quadruple transgenic fish line.
1614 **b,** Validation of APEX2-labeled neuronal types in 6-dpf larvae through immunohistochemical
1615 staining (left) and crossing with neuronal type-specific reporter lines (right). Representative
1616 fluorescent images show APEX2-conjugated TagRFP signals (top), immunofluorescence or
1617 GFP signals in reporter fish lines (middle), and merged channels (bottom).
1618 *Gt(vmat2:GAL4FF);Tg(dbh:GAL4FF;UAS:cytosol-APEX2-TagRFP)* larvae were
1619 immunostained with an anti-tyrosine hydroxylase antibody to validate NE and DA neurons.
1620 *Tg(hcrt:APEX2-TagRFP-NLS)* larvae were immunostained with an anti-hypocretin antibody
1621 to validate Hcrt neurons. *Gt(vmat2:GAL4FF);Tg(dbh:GAL4FF;UAS:cytosol-APEX2-TagRFP)*
1622 larvae were crossed with *Ki(tph2:EGFP)* larvae to validate 5HT neurons.
1623 *Tg(glyt2:MITO-APEX2-TagRFP)* larvae were crossed with *Tg(glyt2:GFP)* larvae to validate
1624 Gly neurons.
1625 **c,** Z-projected whole-brain (left) and expanded (right, c1-c3) fluorescent images of the 6-dpf
1626 multiplexed APEX2-labeled larva used for whole-brain ssEM in this study. Cytosol- and
1627 nucleus-localized APEX2 signals are indicated by white arrows in DA neurons in the OB (top
1628 right, c1) and Hcrt neurons in the hypothalamus (middle right, c2) neurons, and
1629 mitochondria-localized APEX2 signals are outlined with white dashed lines in Gly neurons in
1630 the hindbrain (bottom right, c3).
1631 **d,** Quantification of APEX2-labeled neurons and their ratio (EM/LM) to the theoretical
1632 population size (labeling efficiency). Gly neurons were automatically identified based on
1633 somatic presence of ≥ 4 APEX2-labeled mitochondria, and other APEX2-labeled neurons
1634 were manually counted by experts. Theoretical neuron counts for each neuronal type were
1635 derived from the average of manual counts across three 6-dpf larvae of reporter fish lines. The
1636 number in parentheses indicates the number of identified APEX2-labeled neurons.
1637 C, caudal; L, left; Ri, right; Ro, rostral. LC, locus coeruleus; MO, medulla oblongata; OB,
1638 olfactory bulb; PT, posterior tuberculum; Hc, caudal hypothalamus; Pr, pretectum; RN, raphe
1639 nucleus; NE, noradrenergic; DA, dopaminergic; 5HT, serotonergic; Hcrt, hypocretinergic;
1640 Gly, glycinergic.
1641
1642 **Extended Data Fig. 2 | Workflow for whole-brain ssEM of larval zebrafish.**
1643 **a,** Workflow including *in vivo* confocal fluorescence imaging, fixation, DAB reaction, rOTO
1644 staining, dehydration, resinification, X-ray micro-tomography, ATUM-SEM imaging,
1645 stitching, alignment, correlative light-electron microscopy (CLEM), 3D automatic
1646 reconstruction, manual proofreading, and 3D visualization (see Methods).
1647 **b,** Rendering of 46,536 automatically reconstructed supervoxels in the brain (dorsal view),
1648 with length ranging between 100 – 300 μm.
1649 **c,** Magnified rendering of 1,404 automatically reconstructed periventricular cells in the optic
1650 tectum. The inset displays the soma layer of the optic tectum (yellow).
1651 C, caudal; L, left; V, ventral.
1652
1653 **Extended Data Fig. 3 | Regional distribution of nuclei and perisomatic features of**

diverse cell types.

a,b, Nucleus density distribution across 52 regions in the brain and 7 regions in the retina (**a**). Color-coded regions were annotated through CLEM approach, followed by manual proofreading.

c, UMAP visualization of whole-brain nucleus clustering (176,789 cells) using combined 8-dimensional deep-learned and 13 traditional features (see Methods). All nuclei were manually proofread after automated segmentation, resulting in optimal 3D morphological reconstruction. Based on APEX2-labeling, 4,019 Gly neurons were automatically identified, and 309 neurons of NM types were manually annotated by experts ($n_{LC\text{-}NE}$ = 12, $n_{MO\text{-}NE}$ = 54, $n_{OB\text{-}DA}$ = 38, $n_{PT\text{-}DA}$ = 22, $n_{Hc\text{-}DA}$ = 45, $n_{Pr\text{-}5HT}$ = 9, $n_{RN\text{-}5HT}$ = 117, n_{Hcrt} = 12). In addition, 511 vasculature-associated cells, including endothelial cells (ECs), pericytes (PCs), and red blood cells (RBCs), were manually annotated (n_{EC} = 383, n_{PC} = 84, n_{RBC} = 44) based on their location and perisomatic features. Inset: vasculature-associated cells tending to aggregate. 21 nuclei located at dataset boundaries were excluded from clustering due to incomplete morphologies. Among all reconstructed nuclei, 70,114 cells, whose automatically reconstructed supervoxels possessed at least one synapse, are presumed as neurons, and the remaining are presumed to be glial cells, or neurons which processes were not well automatically reconstructed.

d, Rendering of nuclei from diverse cell types. Shallow grooves and infoldings are indicated by black arrows on the nuclei of LC-NE and Gly neurons, respectively. The irregular nuclear morphologies of two cells with undefined types are shown, suggesting greater diversity of nuclear morphology.

e-l, Comparisons of perisomatic features between APEX2-labeled neurons and a 10-fold number of their adjacent unlabeled cells. Left, nucleus-to-soma volume ratio *vs* somatic mitochondrial density. Right, UMAP visualization of cell clustering using combined deep-learned and traditional features of their nuclei and somata. Cell numbers are shown in parentheses.

C, caudal; L, left. See also Supplementary Tables 1,2,3.

Extended Data Fig. 4 | Soma location of diverse types of APEX2-labeled NM neurons.

Corresponding 33-nm EM sections (64 × 64 nm^2 per pixel) containing representative APEX2-labeled neurons shown in Fig. 2b. Sections are arranged left-to-right and top-to-bottom, following the rostral-caudal axis. Exact positions along the rostral-caudal axis are indicated in the bottom-right schematic diagram. APEX2-labeled neurons with different types are indicated by dashed circles, color-coded according to their neuronal types. Black asterisks denote the exact APEX2-labeled neurons shown in Fig. 2b.

L, left; V, ventral.

Extended Data Fig. 5 | Comparisons of PSD thickness/volume of Glu and GABA synapses annotated by APEX2 labeling.

a, Design of the plasmid *5×UAS-2×Cox8a-APEX2-TagRFP*, which was injected into *Tg(vglut2a:GAL4FF)* and *TgBAC(gad1b:GAL4-VP16)* eggs to specifically label mitochondria in Glu and GABA neurons, respectively.

b,c, Representative EM images of APEX2-labeld mitochondria in axon terminals of Glu (**b**)

and GABA (**c**) neurons. Red dashed lines: APEX2-labeled mitochondria; asterisks: SVs; yellow arrows: juxtaposed PSDs in postsynaptic cells.

d, Comparisons of PSD ultrastructural features between Glu (n = 90) and GABA (n = 102) synapses. PSD thickness was estimated from the diameter of its maximum inscribed sphere. Dashed lines indicate the average values of PSD thickness (horizontal) and volume (vertical). $P_{thickness} = 0.5365$, $P_{volume} = 0.0943$ (Mann Whitney test).

Extended Data Fig. 6 | Comparable whole-brain distributions of PSDs, SVs and mitochondria.

a-c, Density distributions of PSDs (**a**), SVs (**b**), and mitochondria (**c**) across 52 brain regions.

d-f, Pairwise linear regression analysis among PSD density, SV density, and mitochondria density. The solid red lines represent the fitted regression line, and the dashed red lines indicate the 95% confidence interval of the fit. Each circle represents individual brain regions. SV density *vs* PSD density (**d**): $Y = 0.6092 \times X + 12.86$, $R^2 = 0.9398$, $P < 0.0001$; Mitochondria density *vs* SV density (**e**): $Y = 0.7542 \times X + 100.9$, $R^2 = 0.8454$, $P < 0.0001$; Mitochondria density *vs* PSD density (**f**), $Y = 0.4644 \times X + 107.7$, $R^2 = 0.8118$, $P < 0.0001$. See also Supplementary Tables 4,5,6 and Supplementary Video 3.

Extended Data Fig. 7 | Single-cell morphology of diverse types of NM neurons.

a, Workflow for reconstructing mesoscopic single-cell morphologies, adapted from Du et al.[20], with key steps including micro-injection, screening, *in vivo* confocal imaging, manual skeleton tracing, and registration with the mesoscopic brain template.

b-e, Representative examples of mesoscopic single-cell morphologies of diverse NM types, including NE (**b**), DA (**c**), 5HT (**d**), and Hcrt (**e**) neurons. Black arrows indicate somata. The predominantly innervated regions (highlighted in light blue) are shown in parentheses. Left, lateral view; middle, dorsal view; right, zoomed-in morphology (dorsal view).

D, dorsal; L, left; Ro, rostral.

Extended Data Fig. 8 | Reconstruction and synaptic input mapping of a Mauthner cell.

a, Rendering of a right M-cell's soma, lateral dendrites, ventral dendrites, and proximal axon, as well as somatodendritic synaptic input sites (small violet dots, $n_{synapse} = 1{,}966$). Both the morphology and synapses were manually verified based on automatic segmentation results. The axonal branch is not fully displayed.

b, Representative EM image (4×4 nm^2 per pixel) of the M-cell's soma shown in **a**. The nucleus and cytosol are labeled in red and yellow, respectively.

c, Zoom-in view of the dashed rectangle region in **b**, showing synapses formed multiple presynaptic neurons (color coded) at the M-cell's soma.

L, left; Ri, right; D, dorsal; V, ventral. See also Supplementary Video 5.

Extended Data Fig. 9 | Reconstructions of dendritic synaptic inputs of the LC-NE neurons #1/2/4/5.

a, 2D spatial distribution of dendritic synaptic inputs on the LC-NE neurons #1/2/4/5. Each dot represents a single synaptic input site, color-coded by the modality of PNs (Sensory-related, blue; Motor-related, magenta). Gray dots indicate synaptic sites untraced or

traced but not yet reached soma. The distance between each dot and the soma represents the path length from each input site to the soma.

b, Numbers of dendritic synaptic inputs for individual LC-NE neurons. The number on the top indicate the number of all synapses for each neuron.

c, Differential distributions of all identified sensory- (blue, n = 104) and motor-related synaptic inputs (magenta, n = 159) of the four LC-NE neurons along dendritic path length, from the soma to distal region. The average distance to the soma are indicated by dashed lines. ****$P < 0.0001$ (Mann Whitney test).

D, dorsal; V, ventral.

Extended Data Fig. 10 | Spatial difference of PNs for diverse NM types.

a, Schematic illustrating the soma location of NM neurons displayed in **b-d**.

b-d, Rendering of representative DA (green) and 5HT (blue) neurons with their partially reconstructed PNs (gray). Only synapses successfully traced back to their PN somata are shown. PNs of the OB-DA neuron (**b**) were traced separately, whereas PNs of the PT-DA (**c**) and RN-5HT (**d**) neurons were identified during the reconstruction of the five LC-NE neurons' inputs, indicating their identity as inter-CPNs across distinct monoaminergic systems. The number of neurons are indicated by the numbers in parentheses.

C, caudal; L, left.

Extended Data Fig. 11 | Reconstructions of PNs for the LC-NE neurons #1/2/4/5.

a-d, Rendering of EM-reconstructed PNs and corresponding LC-NE neuron #1 (**a**), #2 (**b**), #4 (**c**), or #5 (**d**). The numbers of PNs with E/I composition and the numbers of corresponding synapses formed by these PNs on the targeted LC-NE neuron are shown in parentheses. Notably, two Hcrt neurons (**c**, magenta) with nuclear-localized APEX2 specifically targeted the LC-NE neuron #4, rather than other LC-NE neurons.

Ro, rostral; V, ventral.

1770 **SUPPLEMENTARY INFORMATION**
1771
1772 **SUPPLMENTARY TABLES:**

1773 **Supplementary Table 1 |** Standardized nomenclature of brain regions

1774 **Supplementary Table 2 |** Nucleus count and density across brain regions

1775 **Supplementary Table 3 |** Perisomatic features of multiple APEX2-labeled neurons

1776 **Supplementary Table 4 |** PSD count and density across brain regions

1777 **Supplementary Table 5 |** SV count and density across brain regions

1778 **Supplementary Table 6 |** Mitochondria count and density across brain regions
1779
1780 **SUPPLEMENTARY VIDEOS:**

1781 **Supplementary Video 1 |** A whole-brain EM reconstruction in a 6-dpf larva with multiplexed
1782 neuromodulatory-type labeling, including 520 reconstructed neurons of various types,
1783 176,810 nuclei, neural tracts, and vessels in the brain and anterior spinal cord.

1784 *Gt(vmat2:GAL4FF);Tg(dbh:GAL4FF;UAS:cytosol-APEX2-TagRFP);Tg(hcrt:APEX2-TagRF*
1785 *P-NLS);Tg(glyt2:MITO-APEX2-TagRFP)*, 6 dpf

1786 **Supplementary Video 2 |** Multiplexed APEX2-labeled neuronal types, including
1787 LC-NE/MO-NE neurons (cytosol-APEX2), OB-DA/PT-DA/Hc-DA neurons
1788 (cytosol-APEX2), Pr-5HT/RN-5HT neurons (cytosol-APEX2), Hcrt neurons
1789 (nuclear-APEX2), and Gly neurons (mitochondrial-APEX2).

1790 **Supplementary Video 3 |** Whole-brain density distribution of nucleus/PSD/SV/Mitochondria.
1791 The brain regions first appear sequentially along a rostral-to-caudal axis, followed by the
1792 distributions of corresponding components displayed in descending order of density.

1793 **Supplementary Video 4 |** Dendritic reconstruction and input mapping of multiple
1794 monoaminergic neurons.

1795 **Supplementary Video 5 |** Dendritic reconstruction and input mapping of a Mauthner cell.

1796 **Supplementary Video 6 |** Widely-distributed 374 presynaptic neurons from 32 out of 52
1797 brain regions converging onto a single LC-NE neuron.

1798 **Supplementary Video 7 |** Inputome organization of a single LC-NE neuron. Inputs are
1799 categorized as follows. (1) Sensory- *vs* Motor-related presynaptic neurons (PNs). (2)
1800 Excitatory (glutamatergic) *vs* Inhibitory (GABAergic/glycinergic) PNs. (3) Intra-CPNs within
1801 the LC-NE system. (4) Inter-CPNs among NE, DA, and 5HT systems.
1802

1803 **Supplementary Table 1 | Standardized nomenclature of brain regions**

Region_id	Name	Abbr.	Volume (μm^3)
1	Olfactory bulb	OB	552,907.80
2	Pallium	P	1,176,906.63
3	Subpallium	S	954,796.37
4	Preoptic region	Po	759,356.45
5	Optic tract and accessory optic system	OTAOS	986,748.95
6	Pretectum	Pr	669,170.64
7	Epiphysis (Pineal gland)	Ep	110,533.43
8	Habenula	Ha	289,854.83
9	Dorsal thalamus	DT	286,673.99
10	Ventral thalamus	VT	336,431.48
11	Posterior tuberculum	PT	377,980.15
12	Migrated posterior tubercular region	M2	658,202.84
13	Rostral hypothalamus	Hr	1,204,135.20
14	Intermediate hypothalamus	Hi	1,874,093.02
15	Diffuse nucleus of the intermediate hypothalamus	DHi	250,549.79
16	Caudal hypothalamus	Hc	176,238.95
17	Pituitary	Pit	83,580.57
18	Neuropil layer (optic tectum)	NL	2,939,375.09
19	Periventricular cell layer (optic tectum)	PL	3,760,502.17
20	Tegmentum	T	536,864.29
21	Nucleus of medial longitudinal fascicle	nMLF	30,611.07
22	Oculomotor nerve nucleus	nIII	77,251.04
23	Torus longitudinalis	TL	115,042.14
24	Torus semicircularis	TS	1,105,957.84
25	Rhombomere 1	R1	1,829,045.90
26	Trochlear nerve motor nucleus	nIV	50,476.46
27	Interpeduncular nucleus	IPN	196,849.62
28	Superior Raphe	SR	122,206.58
29	Corpus cerebelli	CCe	1,345,996.74
30	Valvula cerebelli	Va	282,478.01
31	Eminentia granularis	EG	270,844.81
32	Lobus caudalis cerebelli	LCa	32,741.70
33	Medial octavolateralis nucleus	MON	274,799.18
34	Rhombomere 2	R2	1,039,406.70
35	Dorsal motor nucleus of trigeminal nerve	nVd	36,112.51
36	Rhombomere 3	R3	897,971.87
37	Ventral motor nucleus of trigeminal nerve	nVv	16,845.30
38	Inferior raphe	IR	32,603.36
39	Rhombomere 4	R4	891,197.12
40	Rhombomere 5	R5	1,038,459.75
41	Medial vestibular nucleus	MVN	35,611.76

42	Tangential vestibular nucleus	TVN	30,629.58
43	Rostral facial nerve motor nucleus and octavolateralis efferent neurons	nVIIr/OLer	68,704.18
44	Rostral motor nucleus of abducens nerve	nVIr	6,896.53
45	Rhombomere 6	R6	1,048,429.95
46	Caudal facial nerve motor nucleus and octavolateralis efferent neurons	nVIIc/OLec	22,639.00
47	Caudal motor nucleus of abducens nerve	nVIc	14,460.40
48	Rhombomere 7	R7	930,447.61
49	Rhombomere 8	R8	1,964,286.62
50	Glossopharyngeal/Vagal nerve motor nucleus	nIX/X	188,459.61
51	Vagal lobe	VLo	15,311.87
52	Inferior olive	IO	37,314.70
53	Outer nuclear layer	ONL	1,935,701.58
54	Outer plexiform layer	OPL	218,800.10
55	Inner nuclear layer	INL	1,811,315.73
56	Inner plexiform layer	IPL	642,129.04
57	Retinal ganglion cell layer	RGCL	447,158.97
58	Ciliary marginal zone	CMZ	88,195.60
59	Optic nerve	ON	8,981.38

1805 **Supplementary Table 2 | Nucleus count and density across brain regions**

Region_id	Name (abbr.)	Count	Density (per 10^3 μm^3)
1	OB	2,937	5.31
2	P	6,056	5.15
3	S	5,380	5.63
4	Po	4,733	6.23
5	OTAOS	2,380	2.41
6	Pr	5,021	7.50
7	Ep	461	4.17
8	Ha	2,020	6.97
9	DT	2,347	8.19
10	VT	2,875	8.55
11	PT	2,541	6.72
12	M2	1,738	2.64
13	Hr	4,398	3.65
14	Hi	6,934	3.70
15	DHi	1,589	6.34
16	Hc	1,399	7.94
17	Pit	616	7.37
18	NL	1,489	0.51
19	PL	39,919	10.62
20	T	3,098	5.77
21	nMLF	224	7.32
22	nIII	616	7.97
23	TL	864	7.51
24	TS	6,646	6.01
25	R1	9,401	5.14
26	nIV	503	9.97
27	IPN	524	2.66
28	SR	887	7.26
29	CCe	9,287	6.90
30	Va	2,184	7.73
31	EG	2,233	8.24
32	LCa	314	9.59
33	MON	467	1.70
34	R2	5,307	5.11
35	nVd	241	6.67
36	R3	4,313	4.80
37	nVv	65	3.86
38	IR	152	4.66
39	R4	3,822	4.29
40	R5	5,856	5.64
41	MVN	155	4.35
42	TVN	70	2.29

43	nVIIr/OLer	488	7.10
44	nVIr	25	3.63
45	R6	5,376	5.13
46	nVIIc/OLec	130	5.74
47	nVIc	36	2.49
48	R7	5,031	5.41
49	R8	11,784	6.00
50	nIX/X	1,430	7.59
51	VLo	96	6.27
52	IO	267	7.16
53	ONL	23,576	12.18
54	OPL	1,122	5.13
55	INL	38,063	21.01
56	IPL	89	0.14
57	RGCL	6,988	15.63
58	CMZ	1,051	11.92
59	ON	21	2.34

1806

1807 **Supplementary Table 3 | Perisomatic features of multiple APEX2-labeled neurons**

	LC-NE neurons	MO-NE neurons	OB-DA neurons	PT-DA neurons	Hc-DA neurons	Pr-5HT neurons	RN-5HT neurons	Hcrt neurons	Gly neurons
Soma volume (μm^3)	314 (131)	116 (79.0)	106 (99.5)	303 (111)	92.8 (76.5)	104 (86.5)	139 (103)	137 (103)	82.3 (77.5)
Soma surface area (μm^2)	344 (180)	158 (126)	161 (148)	367 (169)	149 (139)	165 (147)	201 (157)	190 (165)	138 (130)
Soma volume/surface ratio (μm)	0.902 (0.710)	0.732 (0.617)	0.658 (0.675)	0.824 (0.658)	0.614 (0.552)	0.630 (0.591)	0.685 (0.652)	0.720 (0.627)	0.595 (0.598)
Soma sphericity	0.648 (0.687)	0.730 (0.701)	0.674 (0.708)	0.595 (0.669)	0.666 (0.632)	0.652 (0.647)	0.643 (0.679)	0.677 (0.652)	0.663 (0.682)
Soma/convex hull area ratio	1.05 (1.08)	1.01 (1.07)	1.01 (1.04)	1.09 (1.05)	1.04 (0.972)	1.08 (1.08)	1.01 (1.05)	1.12 (1.09)	1.04 (1.04)
Soma/convex hull volume ratio	0.686 (0.737)	0.731 (0.765)	0.694 (0.738)	0.637 (0.687)	0.681 (0.592)	0.693 (0.705)	0.650 (0.720)	0.758 (0.694)	0.712 (0.712)
Soma area minus convex hull area (μm^2)	14.8 (12.7)	1.13 (8.20)	-3.38 (3.28)	32.0 (-15.6)	3.71 (-22.1)	11.6 (9.99)	-0.776 (4.84)	20.0 (11.0)	3.41 (0.745)
Convex hull volume minus soma volume (μm^3)	148 (48.7)	45.1 (25.0)	57.0 (40.8)	171 (84.9)	49.0 (75.6)	48.3 (37.8)	75.9 (45.8)	43.9 (54.2)	35.8 (38.0)
Soma elongation ratio	4.64 (4.42)	3.00 (3.35)	3.92 (3.24)	5.68 (5.38)	3.27 (6.95)	4.15 (4.74)	5.22 (5.07)	3.33 (4.88)	4.65 (4.06)
Soma radial range (μm)	7.88 (4.48)	4.08 (3.25)	4.49 (3.60)	7.41 (5.42)	3.81 (5.66)	4.83 (4.73)	7.04 (4.52)	4.19 (4.16)	4.98 (4.41)
Soma normalized max radius	3.43 (2.25)	2.17 (1.73)	2.47 (1.89)	2.74 (1.85)	1.92 (30.0)	2.70 (3.82)	5.90 (2.80)	1.61 (2.79)	4.33 (4.55)
Soma normalized min radius	0.0337 (0.0486)	0.0723 (0.0598)	0.0354 (0.0548)	0.0140 (0.0575)	0.0544 (0.176)	0.0372 (0.0426)	0.0351 (0.0469)	0.0459 (0.0468)	0.0412 (0.0502)
Soma eccentricity	0.833 (0.742)	0.776 (0.792)	0.820 (0.777)	0.842 (0.757)	0.776 (0.801)	0.774 (0.804)	0.823 (0.787)	0.815 (0.769)	0.845 (0.806)
Nucleus volume (μm^3)	117 (79.5)	78.4 (58.4)	77.9 (71.3)	128 (77.0)	64.8 (55.3)	66.6 (63.0)	78.5 (68.0)	91.4 (71.7)	57.8 (56.7)
Nucleus surface area (μm^2)	126 (96.3)	94.3 (77.7)	96.4 (90.7)	141 (93.7)	84.6 (77.8)	90.1 (85.1)	100 (91.9)	105 (90.8)	81.1 (79.6)
Nucleus volume/surface ratio (μm)	0.920 (0.820)	0.831 (0.737)	0.808 (0.782)	0.901 (0.815)	0.762 (0.710)	0.741 (0.741)	0.779 (0.739)	0.866 (0.782)	0.711 (0.710)
Nucleus sphericity	0.913 (0.926)	0.939 (0.923)	0.915 (0.916)	0.867 (0.931)	0.921 (0.904)	0.885 (0.902)	0.881 (0.878)	0.932 (0.917)	0.890 (0.897)
Nucleus/convex hull area ratio	1.01 (1.01)	1.00 (1.00)	1.00 (1.01)	1.01 (1.00)	1.00 (1.01)	1.02 (1.01)	1.01 (1.01)	1.01 (1.00)	1.00 (1.01)

Nucleus/convex hull volume ratio	0.946 (0.961)	0.971 (0.973)	0.965 (0.965)	0.926 (0.966)	0.964 (0.952)	0.937 (0.948)	0.928 (0.928)	0.972 (0.957)	0.946 (0.942)
Nucleus area minus convex hull area (μm^2)	1.55 (0.554)	0.203 (0.279)	0.364 (0.770)	1.79 (0.326)	0.0976 (0.612)	2.06 (0.465)	0.588 (0.956)	0.521 (0.0955)	0.201 (0.621)
Convex hull volume minus nucleus volume (μm^3)	6.72 (3.32)	2.35 (1.41)	2.88 (2.58)	10.4 (2.62)	2.51 (2.91)	4.53 (3.46)	6.00 (5.38)	2.65 (3.33)	3.24 (3.61)
Nucleus elongation ratio	2.05 (1.94)	1.73 (2.02)	2.21 (2.34)	2.46 (2.20)	1.97 (2.15)	2.36 (2.40)	2.57 (3.10)	1.84 (3.37)	2.38 (2.23)
Nucleus radial range (μm)	1.93 (1.58)	1.45 (1.52)	1.98 (1.81)	2.54 (1.58)	1.61 (1.70)	1.88 (1.86)	2.28 (2.12)	1.66 (1.77)	1.90 (1.75)
Nucleus normalized max radius	0.508 (0.540)	0.521 (0.619)	0.676 (0.626)	0.649 (0.608)	0.560 (0.690)	0.606 (0.742)	0.734 (0.855)	0.538 (0.751)	0.726 (0.677)
Nucleus normalized min radius	0.0703 (0.0928)	0.102 (0.0903)	0.0697 (0.0778)	0.0473 (0.0971)	0.0778 (0.0803)	0.0618 (0.0724)	0.0491 (0.0683)	0.0856 (0.0896)	0.0691 (0.0758)
Nucleus eccentricity	0.601 (0.659)	0.697 (0.702)	0.720 (0.718)	0.714 (0.669)	0.738 (0.739)	0.700 (0.701)	0.775 (0.732)	0.671 (0.707)	0.758 (0.716)
Mitochondrial count	165 (13.1)	14.0 (6.48)	9.40 (9.02)	66.3 (5.98)	15.4 (8.06)	5.40 (6.06)	26.2 (9.02)	12.6 (7.38)	6.30 (4.38)
Mitochondrial density per 1 μm^3 soma volume	0.547 (0.0847)	0.120 (0.0803)	0.0838 (0.0912)	0.219 (0.0494)	0.181 (0.106)	0.0528 (0.0671)	0.175 (0.0784)	0.0974 (0.0704)	0.0745 (0.0555)
Mitochondrial density per 1 μm^3 nucleus volume	1.42 (1.47)	0.177 (0.109)	0.117 (0.153)	0.520 (0.0732)	0.243 (0.145)	0.0806 (0.0931)	0.318 (0.122)	0.146 (0.102)	0.107 (0.0758)
Nucleus/soma volume ratio	0.386 (0.640)	0.684 (0.750)	0.741 (0.724)	0.425 (0.712)	0.731 (0.731)	0.653 (0.733)	0.585 (0.683)	0.667 (0.703)	0.710 (0.740)

Data are presented as mean values, with values in parentheses representing unlabeled cells adjacent to APEX2-labeled neurons. See Fig. 2e and Extended Data Fig. 3e-l for cell numbers, and Methods for calculation details.

1812 **Supplementary Table 4 | PSD count and density across brain regions**

Region_id	Name (abbr.)	Count	Density (per 10^3 μm^3)
1	OB	168,961	305.59
2	P	619,202	526.13
3	S	570,921	597.95
4	Po	397,593	523.59
5	OTAOS	969,580	982.60
6	Pr	185,228	276.80
7	Ep	5,371	48.59
8	Ha	74,603	257.38
9	DT	51,797	180.68
10	VT	59,776	177.68
11	PT	194,962	515.80
12	M2	890,300	1,352.62
13	Hr	1,248,748	1,037.05
14	Hi	2,269,327	1,210.89
15	DHi	47,967	191.45
16	Hc	29,554	167.69
17	Pit	6,949	83.14
18	NL	6,274,593	2,134.67
19	PL	143,460	38.15
20	T	488,299	909.54
21	nMLF	4,158	135.83
22	nIII	20,325	263.10
23	TL	10,079	87.61
24	TS	997,075	901.55
25	R1	1,817,808	993.86
26	nIV	3,156	62.52
27	IPN	235,891	1,198.33
28	SR	31,382	256.79
29	CCe	543,830	404.04
30	Va	55,456	196.32
31	EG	94,508	348.94
32	LCa	256	7.82
33	MON	387,594	1,410.46
34	R2	1,024,545	985.70
35	nVd	6,723	186.17
36	R3	768,601	855.93
37	nVv	17,612	1,045.51
38	IR	11,246	344.93
39	R4	746,597	837.75
40	R5	660,500	636.04
41	MVN	15,087	423.65
42	TVN	31,957	1,043.34

43	nVIIr/OLer	10,745	156.40
44	nVIr	8,262	1,197.99
45	R6	750,372	715.71
46	nVIIc/OLec	1,141	50.40
47	nVIc	18,099	1,251.63
48	R7	864,232	928.83
49	R8	1,309,422	666.61
50	nIX/X	82,721	438.93
51	VLo	3,171	207.09
52	IO	17,618	472.15

1813

1814 **Supplementary Table 5 | SV count and density across brain regions**

Region_id	Name (abbr.)	Count	Density (per 10^3 μm^3)
1	OB	157,880	285.54
2	P	440,095	373.94
3	S	418,483	438.30
4	Po	274,409	361.37
5	OTAOS	567,745	575.37
6	Pr	107,340	160.41
7	Ep	6,561	59.36
8	Ha	38,386	132.43
9	DT	28,278	98.64
10	VT	34,647	102.98
11	PT	111,957	296.20
12	M2	578,311	878.62
13	Hr	756,460	628.22
14	Hi	1,493,329	796.83
15	DHi	28,689	114.50
16	Hc	20,016	113.57
17	Pit	11,688	139.84
18	NL	3,864,426	1,314.71
19	PL	81,328	21.63
20	T	325,770	606.80
21	nMLF	1,988	64.94
22	nIII	11,687	151.29
23	TL	6,317	54.91
24	TS	584,917	528.88
25	R1	1,091,715	596.88
26	nIV	1,351	26.76
27	IPN	223,406	1,134.91
28	SR	18,389	150.47
29	CCe	412,867	306.74
30	Va	51,639	182.81
31	EG	45,662	168.59
32	LCa	137	4.18
33	MON	179,624	653.66
34	R2	587,247	564.98
35	nVd	4,383	121.37
36	R3	439,578	489.52
37	nVv	9,836	583.90
38	IR	8,031	246.32
39	R4	447,452	502.08
40	R5	396,779	382.08
41	MVN	9,154	257.05
42	TVN	17,689	577.51

43	nVIIr/OLer	7,489	109.00
44	nVIr	5,165	748.93
45	R6	457,744	436.60
46	nVIIc/OLec	814	35.96
47	nVIc	11,255	778.33
48	R7	516,297	554.89
49	R8	809,742	412.23
50	nIX/X	50,822	269.67
51	VLo	2,377	155.24
52	IO	12,457	333.84

1815

1816 **Supplementary Table 6 | Mitochondria count and density across brain regions**

Region_id	Name (abbr.)	Count	Density (per 10^3 μm^3)
1	OB	146,644	265.22
2	P	365,682	310.71
3	S	364,324	381.57
4	Po	247,663	326.15
5	OTAOS	535,443	542.63
6	Pr	133,626	199.69
7	Ep	11,706	105.90
8	Ha	58,557	202.02
9	DT	45,091	157.29
10	VT	47,103	140.01
11	PT	107,722	284.99
12	M2	411,387	625.02
13	Hr	617,761	513.03
14	Hi	1,115,733	595.35
15	DHi	30,243	120.71
16	Hc	34,030	193.09
17	Pit	17,205	205.85
18	NL	2,582,241	878.50
19	PL	265,164	70.51
20	T	303,911	566.09
21	nMLF	3,942	128.78
22	nIII	18,408	238.29
23	TL	15,109	131.33
24	TS	509,154	460.37
25	R1	905,849	495.26
26	nIV	4,828	95.65
27	IPN	217,883	1,106.85
28	SR	27,805	227.52
29	CCe	399,534	296.83
30	Va	65,467	231.76
31	EG	73,700	272.11
32	LCa	1,190	36.35
33	MON	251,781	916.24
34	R2	490,509	471.91
35	nVd	6,031	167.01
36	R3	402,701	448.46
37	nVv	6,147	364.91
38	IR	13,723	420.91
39	R4	427,100	479.24
40	R5	413,002	397.71
41	MVN	12,173	341.83
42	TVN	25,790	842.00

43	nVIIr/OLer	14,259	207.54
44	nVIr	4,869	706.01
45	R6	497,382	474.41
46	nVIIc/OLec	5,806	256.46
47	nVIc	12,623	872.94
48	R7	487,363	523.79
49	R8	866,776	441.27
50	nIX/X	54,772	290.63
51	VLo	3,139	205.00
52	IO	15,150	406.01

1819 **Figures**

1820 Fig.1

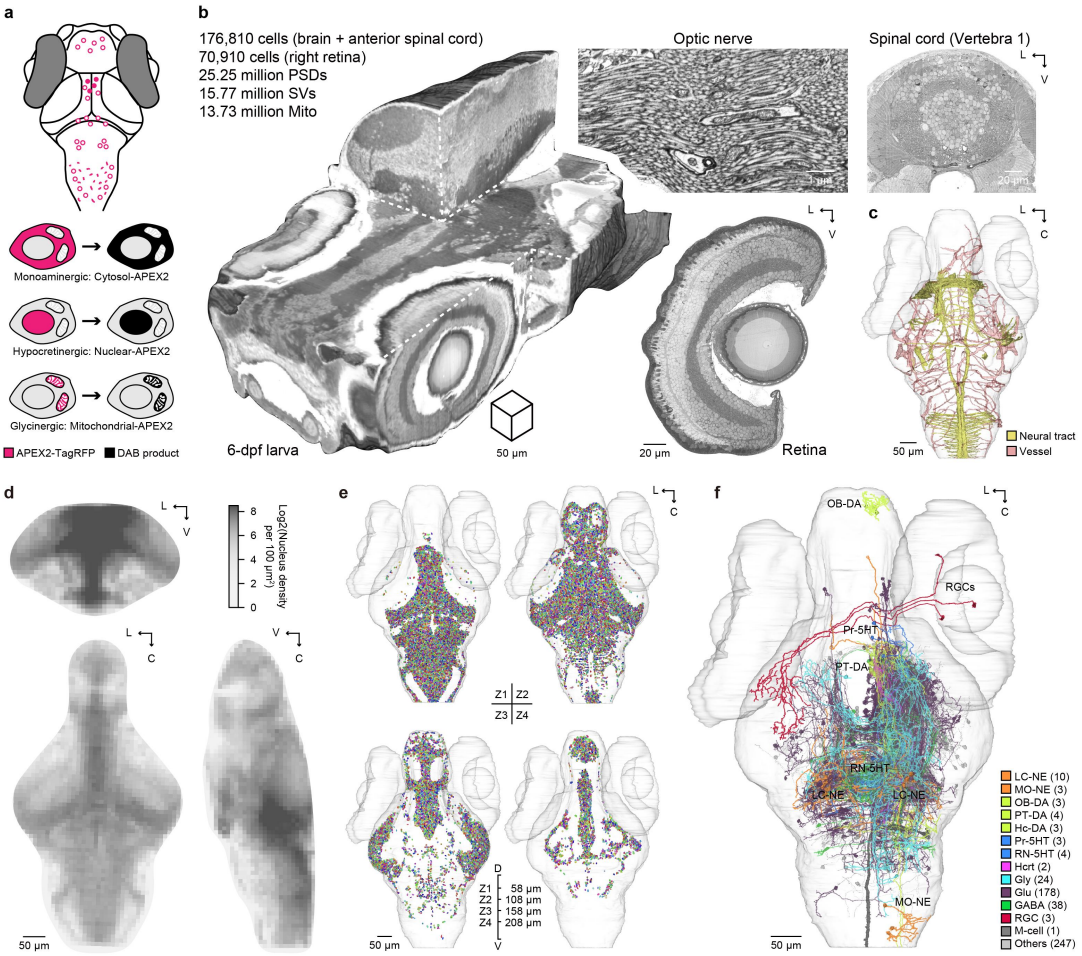

1821

1822

Fig.2

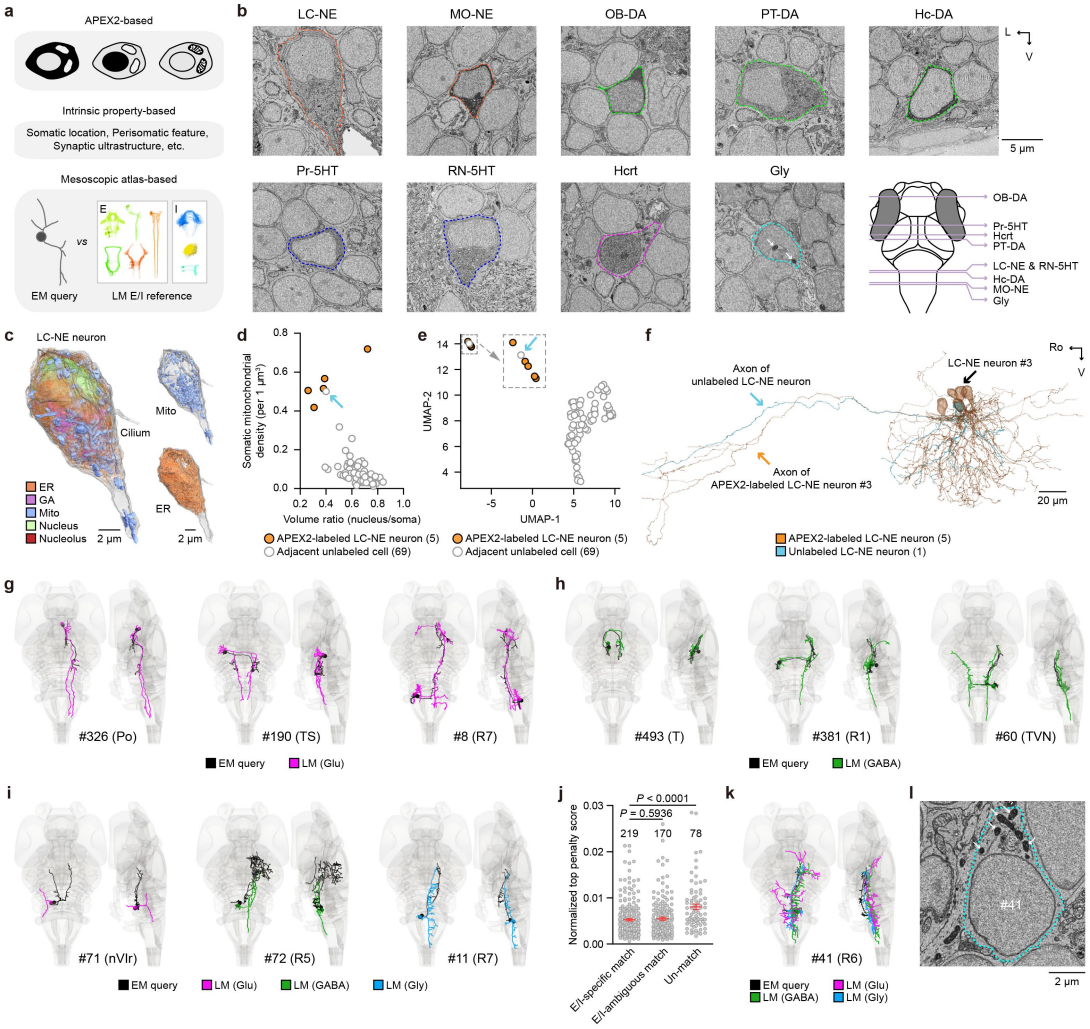
a
APEX2-based
Intrinsic property-based
Somatic location, Perisomatic feature, Synaptic ultrastructure, etc.
Mesoscopic atlas-based
vs
E
I
EM query
LM E/I reference
b
LC-NE
MO-NE
OB-DA
PT-DA
Hc-DA
L
V
5 μm
Pr-5HT
RN-5HT
Hcrt
Gly
OB-DA
Pr-5HT
Hcrt
PT-DA
LC-NE & RN-5HT
Hc-DA
MO-NE
Gly
c
LC-NE neuron
Mito
Cilium
ER
ER
GA
Mito
Nucleus
Nucleolus
2 μm
2 μm
d
Somatic mitochondrial density (per 1 μm³)
Volume ratio (nucleus/soma)
APEX2-labeled LC-NE neuron (5)
Adjacent unlabeled cell (69)
e
UMAP-2
UMAP-1
APEX2-labeled LC-NE neuron (5)
Adjacent unlabeled cell (69)
f
Ro
V
Axon of unlabeled LC-NE neuron
LC-NE neuron #3
Axon of APEX2-labeled LC-NE neuron #3
20 μm
APEX2-labeled LC-NE neuron (5)
Unlabeled LC-NE neuron (1)
g
#326 (Po)
#190 (TS)
#8 (R7)
EM query
LM (Glu)
h
#493 (T)
#381 (R1)
#60 (TVN)
EM query
LM (GABA)
i
#71 (nVIr)
#72 (R5)
#11 (R7)
EM query
LM (Glu)
LM (GABA)
LM (Gly)
j
P < 0.0001
P = 0.5936
219
170
78
Normalized top penalty score
E/I-specific match
E/I-ambiguous match
Un-match
k
#41 (R6)
EM query
LM (Glu)
LM (GABA)
LM (Gly)
l
#41
2 μm

Fig.3

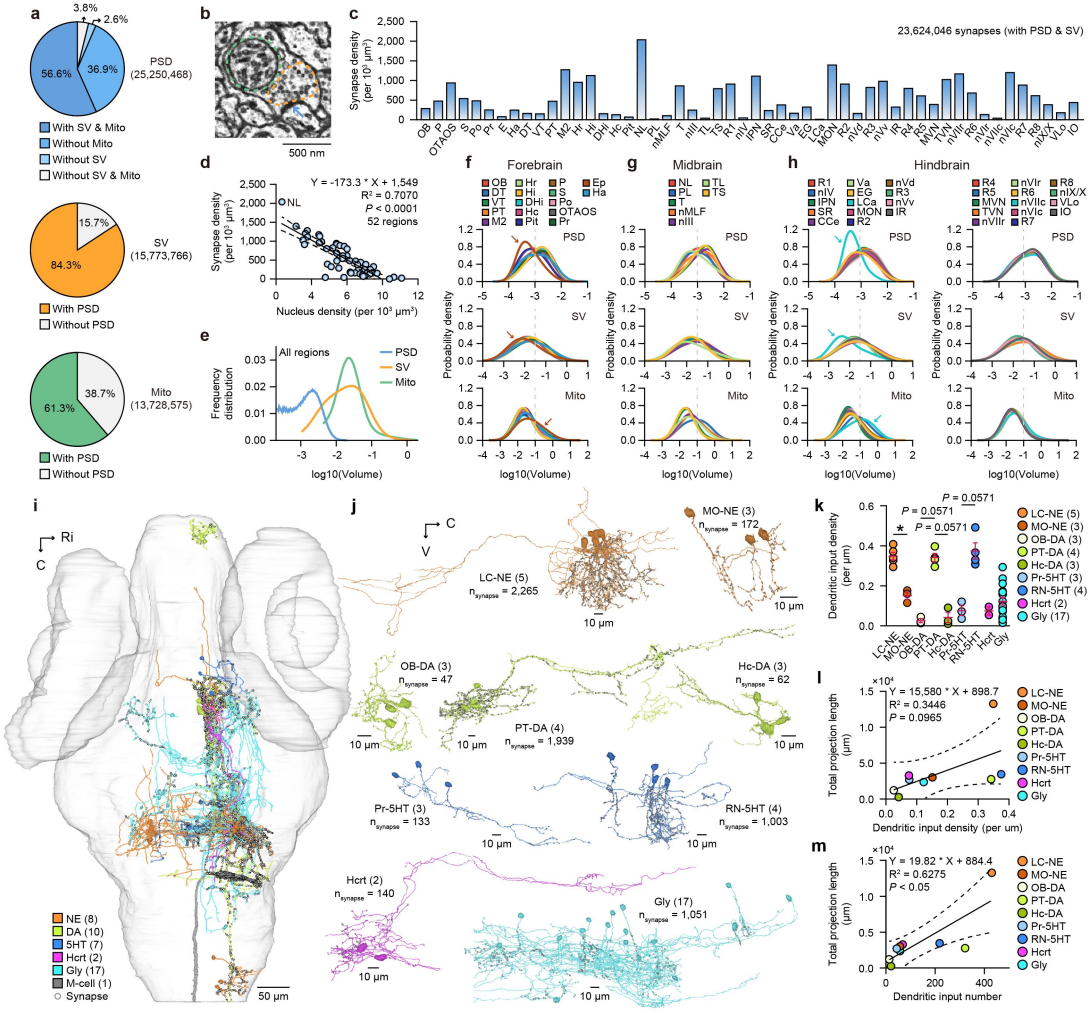
a
3.8%
2.6%
56.6%
36.9%
PSD
(25,250,468)
With SV & Mito
Without Mito
Without SV
Without SV & Mito
15.7%
84.3%
SV
(15,773,766)
With PSD
Without PSD
38.7%
61.3%
Mito
(13,728,575)
With PSD
Without PSD
b
500 nm
c
23,624,046 synapses (with PSD & SV)
Synapse density (per 10³ μm³)
d
Y = -173.3 * X + 1,549
R² = 0.7070
P < 0.0001
52 regions
NL
Synapse density (per 10³ μm³)
Nucleus density (per 10³ μm³)
e
All regions
PSD
SV
Mito
Frequency distribution
log10(Volume)
f
Forebrain
g
Midbrain
h
Hindbrain
PSD
SV
Mito
Probability density
log10(Volume)
i
Ri
C
NE (8)
DA (10)
5HT (7)
Hcrt (2)
Gly (17)
M-cell (1)
Synapse
50 μm
j
C
V
LC-NE (5)
n_synapse = 2,265
MO-NE (3)
n_synapse = 172
OB-DA (3)
n_synapse = 47
PT-DA (4)
n_synapse = 1,939
Hc-DA (3)
n_synapse = 62
Pr-5HT (3)
n_synapse = 133
RN-5HT (4)
n_synapse = 1,003
Hcrt (2)
n_synapse = 140
Gly (17)
n_synapse = 1,051
10 μm
k
P = 0.0571
P = 0.0571
P = 0.0571
Dendritic input density (per μm)
LC-NE (5)
MO-NE (3)
OB-DA (3)
PT-DA (4)
Hc-DA (3)
Pr-5HT (3)
RN-5HT (4)
Hcrt (2)
Gly (17)
l
×10⁴
Y = 15,580 * X + 898.7
R² = 0.3446
P = 0.0965
Total projection length (μm)
Dendritic input density (per um)
m
×10⁴
Y = 19.82 * X + 884.4
R² = 0.6275
P < 0.05
Total projection length (μm)
Dendritic input number

Fig.4

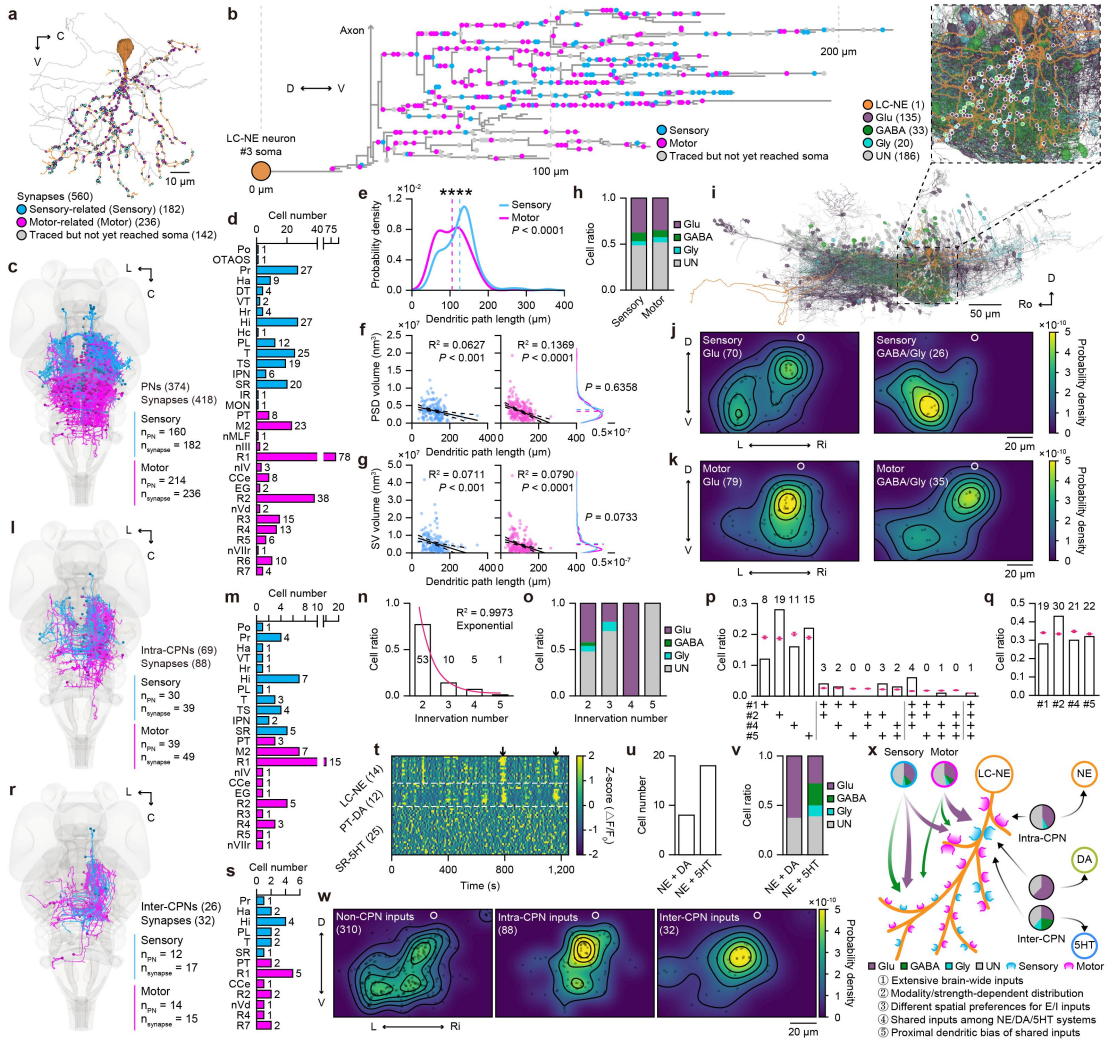
a
b
c
d
e
f
g
h
i
j
k
l
m
n
o
p
q
r
s
t
u
v
w
x
Synapses (560)
Sensory-related (Sensory) (182)
Motor-related (Motor) (236)
Traced but not yet reached soma (142)
LC-NE neuron
#3 soma
Axon
Sensory
Motor
Traced but not yet reached soma
LC-NE (1)
Glu (135)
GABA (33)
Gly (20)
UN (186)
PNs (374)
Synapses (418)
Intra-CPNs (69)
Synapses (88)
Inter-CPNs (26)
Synapses (32)
Cell number
Probability density
Dendritic path length (μm)
PSD volume (nm³)
SV volume (nm³)
Cell ratio
Innervation number
Exponential
Time (s)
Z-score (ΔF/F0)
Non-CPN inputs (310)
Intra-CPN inputs (88)
Inter-CPN inputs (32)
Sensory Glu (70)
Sensory GABA/Gly (26)
Motor Glu (79)
Motor GABA/Gly (35)
NE + DA
NE + 5HT
LC-NE
NE
Intra-CPN
DA
Inter-CPN
5HT
① Extensive brain-wide inputs
② Modality/strength-dependent distribution
③ Different spatial preferences for E/I inputs
④ Shared inputs among NE/DA/5HT systems
⑤ Proximal dendritic bias of shared inputs

Extended Data Figures

Extended Data Fig.1

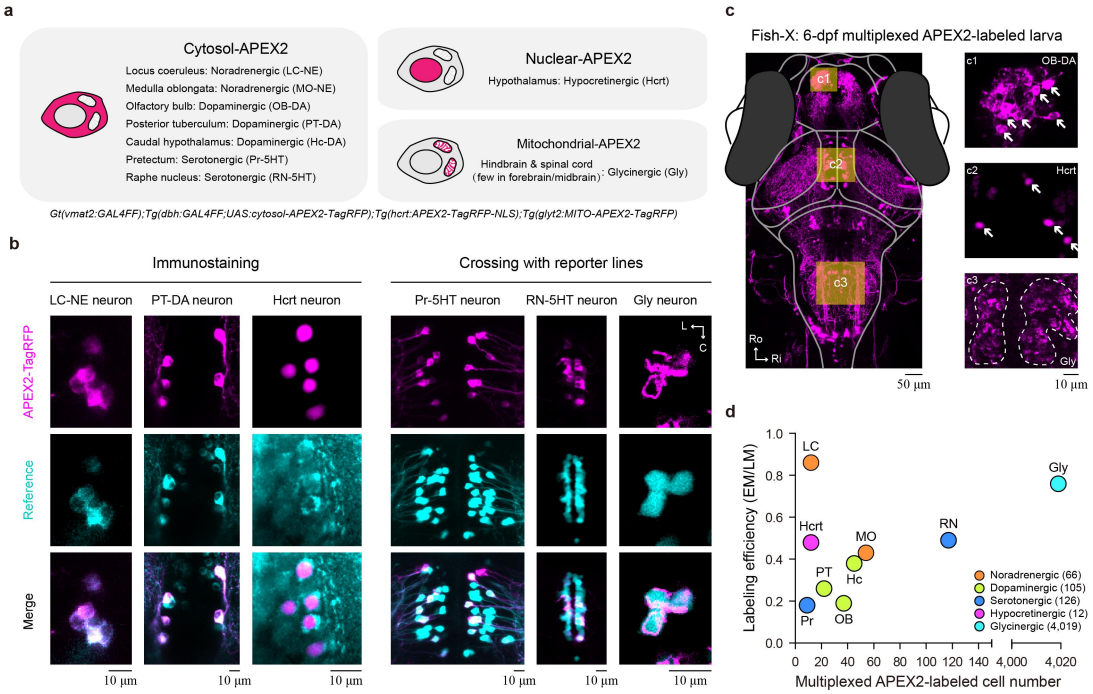

Extended Data Fig.2

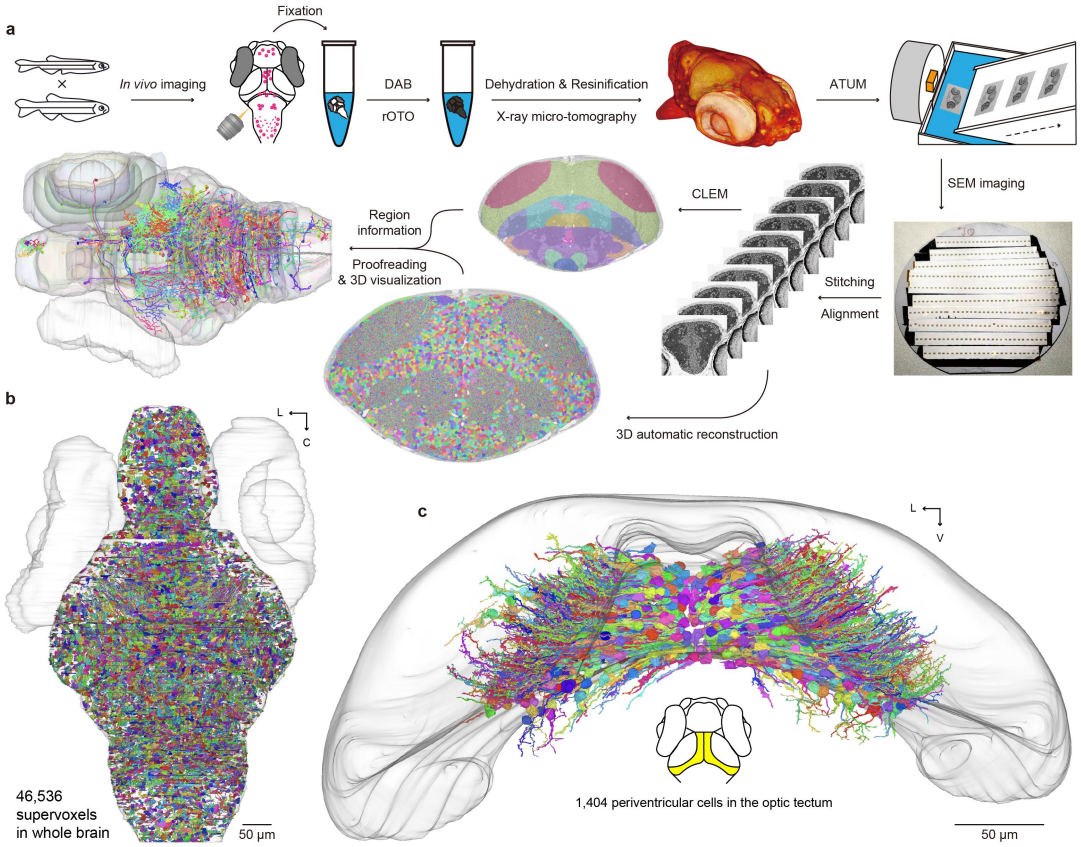

Extended Data Fig.3

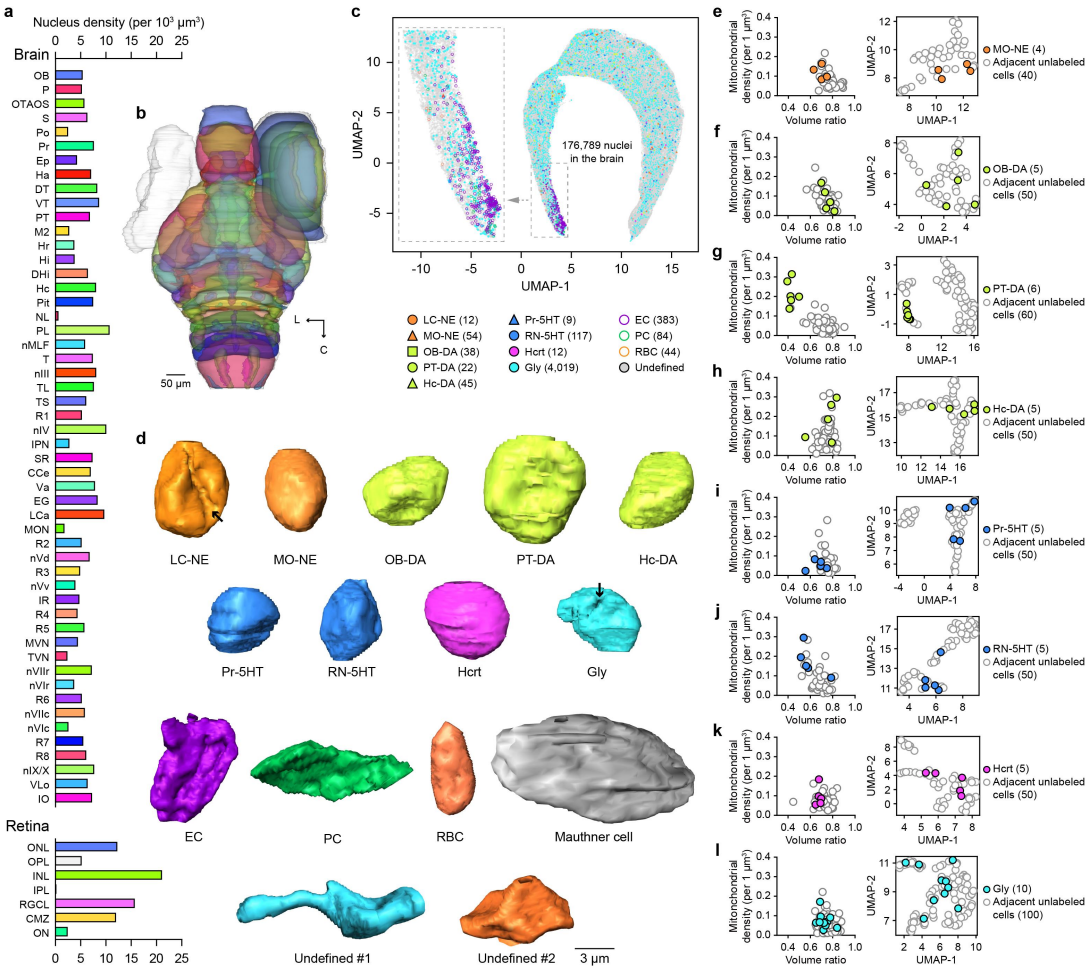

Extended Data Fig.4

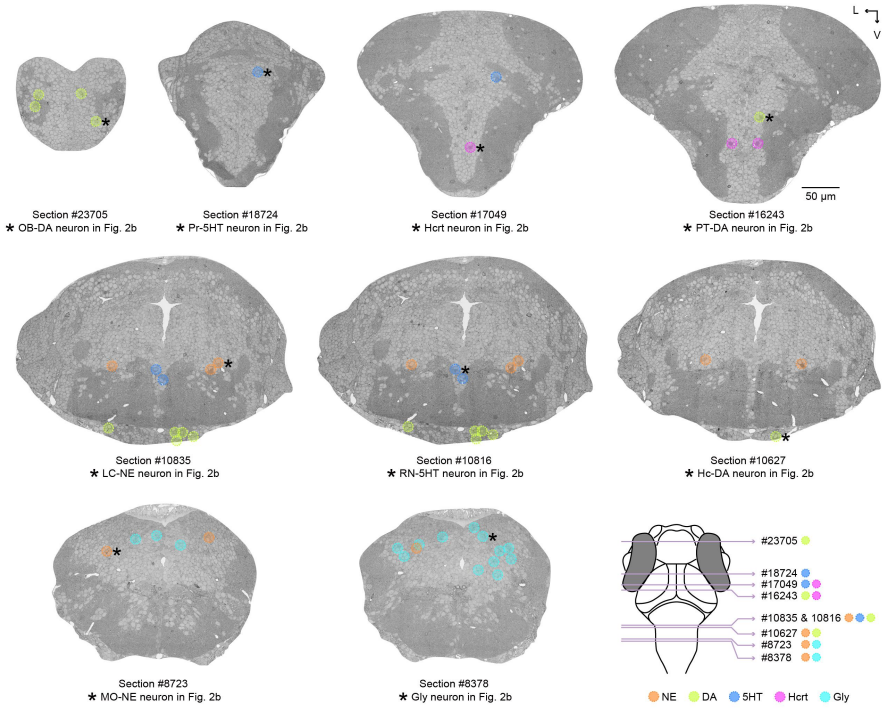

Extended Data Fig.5

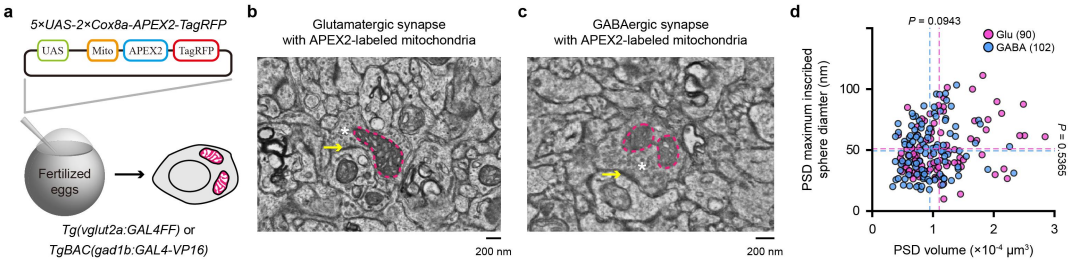

Extended Data Fig.6

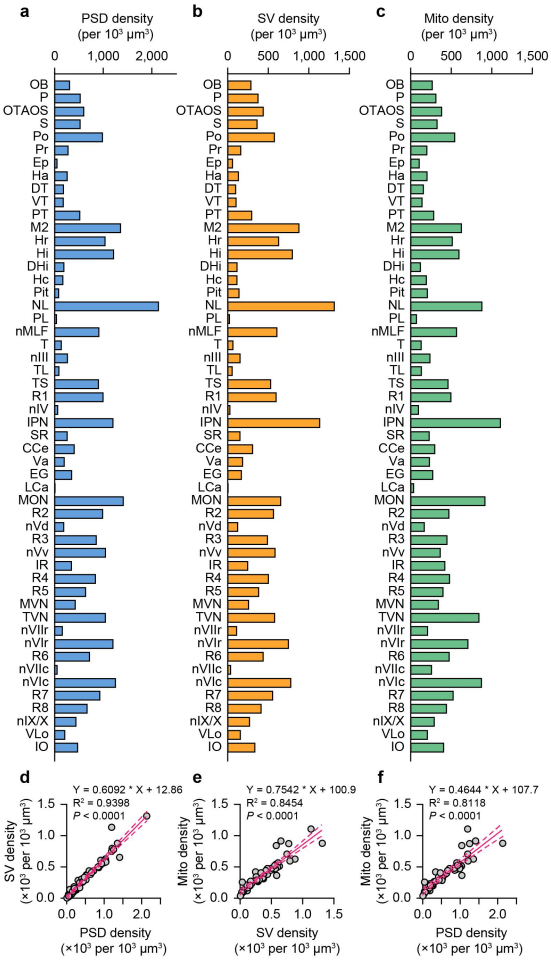

Extended Data Fig.7

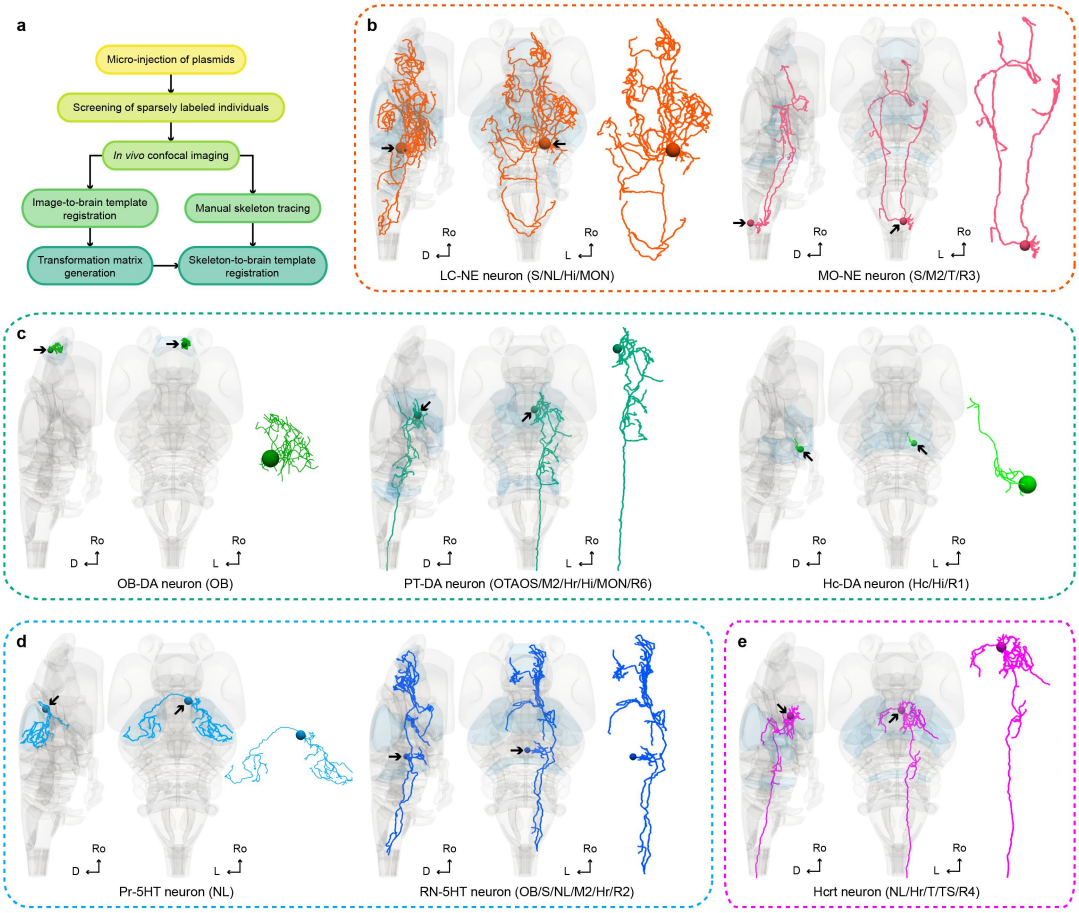

Extended Data Fig.8

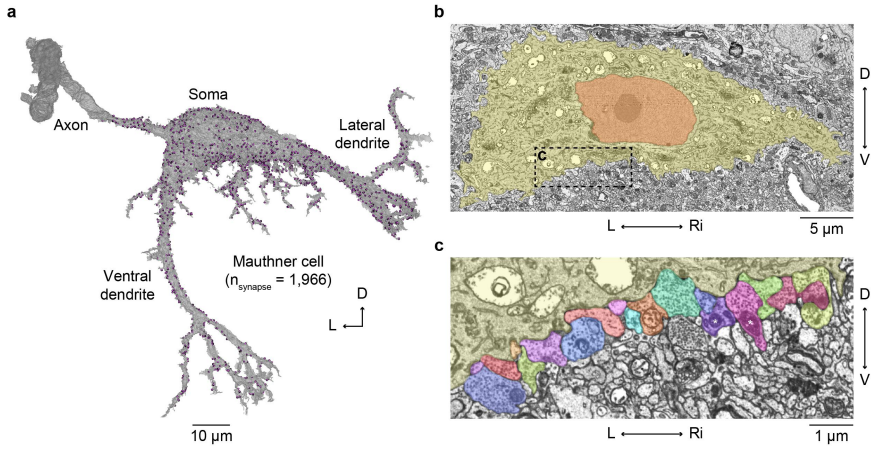

Extended Data Fig.9

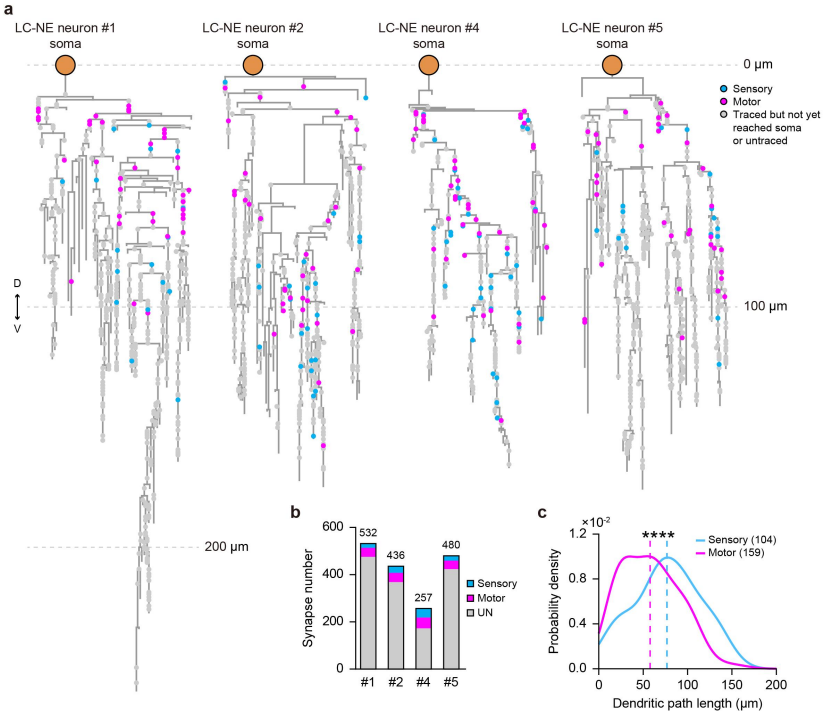

Extended Data Fig.10

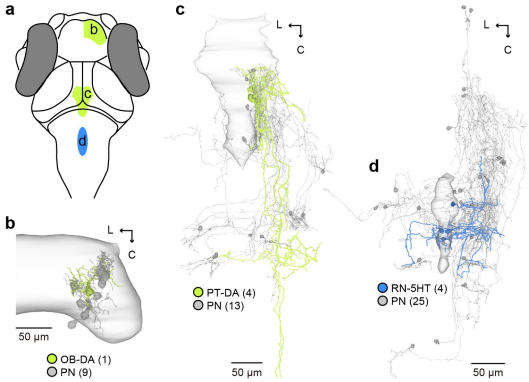
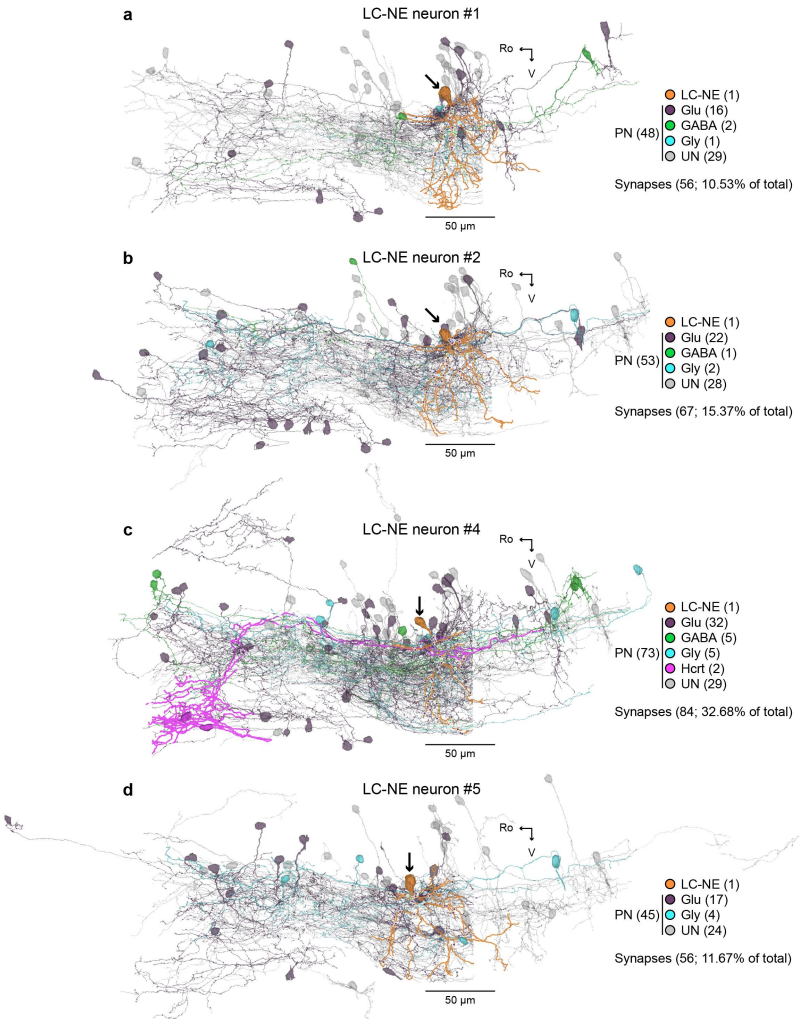
Extended Data Fig.11